

Part I

Literature review

Dragert *et al.* (2001 [11]) carefully analyzed data from 14 GPS sites in Cascadia. They detected a reversed direction of motion, lasting for a few days, at several sites located landward from the locked seismogenic zone. The observed signal propagated parallel to the strike of the subducting slab at around 6 km per day. They fitted the observed displacements with the displacements produced by a fault located at the plate boundary in an elastic half-space, and concluded that the slip must have occurred downdip of the locked and transition zones. The total moment derived from their numerical modelling was equivalent to a $M_w = 6.7$ earthquake. They suggested that deep-slip events like this could play a key role in the stress loading of the seismogenic zone, and therefore trigger megathrust earthquakes.

Obara (2002 [32]) computed the cross correlations of envelope seismograms between pairs of stations of the Hi-net network in southwestern Japan, while moving the time lag between the two traces. It allowed him to identify long coherent signals, with a predominant frequency of 1 to 10 Hz. A rough estimate of the propagation velocity of these tremors led him to conclude that they were propagated by S-wave velocity. The tremors were located in the western part of Shikoku and in the Kii peninsula, near the Mohorovičić discontinuity. Obara speculated that the observed tremors may be a continuous sequence of low frequency earthquakes. Due to the long duration of the tremors and the mobility of the tremor activity, he suggested that the occurrence of tremors may be related to the release of fluids in the subduction zone.

Preston *et al.* (2003 [37]) analyzed first and second arrivals travel times from marine active sources, and first arrival travel times from local earthquakes in Cascadia. They inverted their data for 3D P-wave velocity structure, earthquake locations, and geometry of the reflector. They interpreted the reflector as the Moho of the subducting Juan de Fuca plate. The earthquakes were separated into two groups. The earthquakes in the first group were located in the oceanic mantle, up-dip of the Moho's 45km depth contour, and might be caused by serpentinite dehydration. The earthquakes in the second group occurred in the subducted oceanic crust, down-dip of the Moho's 45km depth contour, and might be caused by basalt-to-eclogite transformation. No other reflector that could correspond to the plate boundary and the upper limit of a low velocity zone was detected.

Rogers and Dragert (2003 [38]) examined a number of seismograph signals in Vancouver Island together and observed tremorlike signals identified by the similarities in their envelopes. These signals were characterized by frequencies between 1 and 5 Hz, pulses of energy, and a duration from a few minutes to several days. Their occurrence was correlated temporally and spatially with slip events on the subduction zone interface. The source depth of the tremors was comprised between 25 and 45 km, which is compatible with a location on the plate interface where the slip was supposed to occur. They named this phenomenon Episodic Tremor and Slip (ETS). They believed that the cause of these tremors could be a shearing source and that fluids may play an important role in their generation.

Obara *et al.* (2004 [33]) observed tiltmeters data in boreholes in western Shikoku, and compared them with tremor activity. They noticed the simultaneous occurrence and migration of slow slip and tremors, with a recurrence interval of approximately six months. They divided the phenomena into two steps, modelled the slow slip by a dislocation on two reverse faults, and found a good agreement between predicted slip and tilt observations. The updip limit of the slip corresponded to the location of the tremors, whereas the downdip limit of the slip corresponded to the junction between the top of the subducting oceanic plate and the continental Moho. They concluded that the coupling phenomenon producing both tremors and slow slip should be located on the plate boundary and be related to the stress accumulation of the locked zone.

Szeliga *et al.* (2004 [47]) used a combination of data from GPS and seismic stations to look for slow slip events in southern Cascadia. The GPS time series from the Pacific Northwest Geodetic Array and the Bay Area Regional Deformation Array were stabilized using a reference set of stations from stable North America. The final time series were then detrended, and offsets due to hardware upgrades, earthquakes, and atmospheric seasonal effects, were removed. Recordings from seismic stations of the Northern California Seismic Network (NCSN) were used to count the number of hours of tremor per week. The authors observed a correlation between the tremor rate and deformation reversals. Slow slip events occur about every 11 months in northern California, and sporadic events were observed in central Oregon. Slow slip events may thus not be confined to the Puget Sound area, but may occur throughout Cascadia.

Sánchez-Sesma and Campillo (2006, [40]) studied the relationship between the Green's function and the cross correlation in an elastic isotropic medium. They assumed an equipartition of elastic plane waves, that is the energy is equally distributed among all possible modes and all possible direction of propagation. The wave field is thus diffuse, and the ratio between The P and the S spatial energy densities is equal to $E_S/E_P = (\alpha/\beta)^2$ in 2D and $E_S/E_P = 2(\alpha/\beta)^3$ in 3D. They considered the case of an SH wave in a 2D medium, the case of P and SV waves in a 2D medium, and the case of the 3D medium. For each case, they computed on one hand the cross correlation of the displacement at a point x and the displacement at a point y , and on the other hand the Green's function between point x and point y . Using the value of the P to S energy ratio, they established that in all three cases the average cross correlation over all directions of motion between two points is proportional to the imaginary part of the Green's function between these two points.

Shelly *et al.* (2006 [44]) used a combination of waveform cross-correlation and double-difference tomography to get a precise location of the source of low-frequency earthquakes (LFE), and a high-resolution velocity structure, in western Shikoku. They observed that the LFEs are located on a plane 5–8 km above the dipping plane of regular seismicity within the subducting plate, and concluded that the LFEs must occur at the plate interface, while regular seismicity begins within the lower part of the crust at shallower depths, and expand upwards the crust as the slab subducts. They also found a zone of high V_P/V_S ratio in the vicinity of the LFEs, which they interpret as high pore-fluid pressure. They hypothesize that the LFEs may be generated by local shear slip accelerations due to local heterogeneities during large slow slip events at the plate interface, and that the high pore-fluid pressure might enable slip by reducing normal effective stress.

Ide *et al.* (2007 [21]) computed cross correlation of low-frequency earthquakes (LFE) waveforms in western Shikoku, and concluded from their predominantly positive distribution that mechanisms of LFEs are very similar. Then, they compared the polarity of regular intraplate earthquake waveforms and stacked LFE waveforms in order to identify the nodal planes of P-wave radiation. Finally, they inverted the moment tensor of a reference LFE using S-waveforms and intraplate earthquakes waveforms as empirical Green's function. The focal mechanism was a shallow dipping thrust fault, consistent with the subduction of the Philippine plate. The fact that this mechanism is consistent with fault models for slow slip events led them to conclude that slow slip, LFEs and tremors must be different manifestation of the same process.

Ide *et al.* (2007 [20]) studied the scaling and spectral behaviour of slow earthquakes (e.g. silent earthquakes, low-frequency earthquakes, low-frequency tremor, slow slip events, and very-low-frequency earthquakes). They observed that their seismic moment is proportional to their duration (and not the cube of the duration, as is the case for regular earthquakes), and that their seismic moment rate is proportional to the inverse of the frequency (and not the inverse of the square of the frequency, as is the case for regular earthquake). They proposed two models to explain this behaviour. In the constant low-stress drop model, the propagation velocity is proportional to the square of the characteristic length. In the diffusional model, the slip is constant and the propagation velocity is proportional of the characteristic length. They conclude that all slow earthquakes are different manifestations of the same physical phenomenon, and constitute a new earthquake category.

Shelly *et al.* (2007 [43]) observed that tremor and low-frequency earthquakes (LFE) had similar frequency content, distinct of the spectra of background noise and regular earthquakes. They used well recorded LFEs in Shikoku as template events, and cross correlated their waveforms with tremor waveforms recorded in the same area. They stacked the corresponding correlation coefficients for the three components of several stations, and identify the tremor waveform as a small LFE if the summed correlation coefficient was higher than a threshold. They found that the events thus detected had a good spatial coherence, and that most of the tremor signal could be explained by a swarm of small LFEs. They concluded that the tremors were generated by the same mechanism that causes LFEs and slow slip, that is fluid enabled shear slip on the plate boundary.

Szeliga *et al.* (2008 [46]) determined the timing and the amplitude of 34 slow slip events throughout the Cascadia subduction zone between 1997 and 2005. They stabilized the GPS time series using a reference set of stations from stable North America. They then modelled the GPS time series by the sum of a linear trend, annual and biannual sinusoids representing seasonal effects (Blewitt and Lavallée, 2002), and Heaviside step functions corresponding to earthquakes and hardware upgrades. The linear system was then solved using a weighted QR decomposition (Nikolaïdis, 2002). Finally, they applied a Gaussian wavelet transform to the residual time series to get the exact timing of the slow slip at each GPS station. The succeeding wavelet basis functions are increasingly sensitive to temporal localization of a given signal, and the onset of faulting appears on the wavelet spectrum as an amplitude spike present over all frequencies. The offset for each slow slip event was then used to invert for the slow slip at depth by assuming a thrust fault slip at each subfault of the plate boundary. An equivalent moment magnitude is thus obtained. The authors noted that the events are disconnected, and short-lived (1 to 7 weeks with a maximum displacement of 1 centimetre), and that they do not extend to the tightly coupled shallower plate interface. No long term event was observed during the time period studied. Finally, the lack of resolvable vertical deformation prevented the authors from giving a constraint on the downdip extent of the slow slip.

Wech and Creager (2008 [50]) computed the cross correlations of envelope seismograms for a set of 20 stations in western Washington and southern Vancouver Island. They performed a grid search over all possible source locations to determine which one minimizes the difference between the maximum cross correlation and the value of the correlogram at the lag time corresponding to the S-wave travel time between two stations. This location method is automated (and thus, less labor intensive), makes use of near real-time regional data, and is less computationally intensive than previously proposed methods. They applied their method to the 2007 and 2008 Episodic Tremor and Slip (ETS) events, and located the epicentres in the region where the plate interface is 30–45 km deep and found a sharp updip boundary of the tremor 75 km east of the downdip edge of the megathrust zone. Moreover, they identified between the two ETS events geodetically undetectable tremor that represents nearly half of the total amount of tremor. They concluded that their location method could help mapping the transition and locked zones of the plate boundary.

Audet *et al.* (2009 [4]) computed receiver functions of teleseismic waves in Vancouver Island, and analyzed the delay times between the forward-scattered P-to-S, and back-scattered P-to-S and S-to-S conversions at two seismic reflectors identified as the top and bottom of the oceanic crust. It allowed them to compute the P-to-S velocity ratio (V_P/V_S) of the layer and the S-wave velocity contrast at both interfaces. The very low Poisson's ratio of the layer could not be explained by the composition, and they interpreted it as evidence for high pore-fluid pressure. They explained the sharp velocity contrast on top of the layer as a low permeability boundary between the oceanic plate and the overriding continental crust. They concluded that the high pore-fluid pressures in the oceanic crust could explain the recurrence of Episodic Tremor and Slip (ETS) events, either by hydrofracturing, either by extending the region of conditionally stable slip.

La Rocca *et al.* (2009 [25]) stacked seismograms over all stations of the array for each component, and for three arrays in Cascadia. They then computed the cross-correlation between the horizontal and the vertical component, and found a distinct and persistent peak at a positive lag time, corresponding to the time between P-wave and S-wave arrivals. Using a standard layered Earth model, and horizontal slowness estimated from array analysis, they computed the depths of the tremor sources. They located the sources near or at the plate interface, with a much better depth resolution than previous methods based on seismic signal envelopes, source scanning algorithm, or small-aperture arrays. They concluded that at least some of the tremor consisted in the repetition of low-frequency events as was the case in Shikoku. A drawback of the method was that it could be applied only to tremor located beneath an array, and coming from only one place for an extended period of time.

Ghosh *et al.* (2010 [16]) used a beam backprojection (BBP) method to detect and locate tremor from seismic recordings of a small-aperture array in the Olympic Peninsula. They observed tremor propagating near-continuously in the slip-parallel direction, at velocities between 30 and 200 km/h, and for distances up to 40 km. They proposed two mechanisms to explain these tremor streaks. In the first model, the slip and the plate dip direction differ by up to $\theta = 35^\circ$. The tremor propagates along slip-parallel striations, corrugations, and ridge-and-groove structures on the fault surface. The long-term front velocity V_L and the short-term streak velocity V_S are related by $\sin \theta = \frac{V_L}{V_S}$. In the second model, periodic breaking of the impermeable caprock increases the pore pressure and creates a pressure gradient that will in turn induce fluid flow along a conduit made available by striations and grooves on the fault plane. However, this last model requires long continuous conduits that seem unlikely. Tremor distribution thus varies over different time scales: along-strike migration of the front at about 10 km/day, rapid tremor reversals at about 10 km/h, and along-slip tremor streaks at about 30-200 km/h. Moreover, the moment release of tremors is distributed among patches.

Ohtani *et al.* (2010 [34]) designed the Network Stain Filter (NSF) to detect transient deformation signals from large-scale geodetic arrays. Contrary to their previous work on the Network Inversion Filter (NIF), there is no need to specify potential sources of deformation. They modelled the position of the GPS station by the sum of the secular velocity, a spatially coherent field, site-specific noise, reference frame errors, and observation errors. The spatial displacement field is modelled by the sum of basis wavelets (the Deslauriers-Dubuc wavelet of degree 3) with time-varying weights. The transient is considered to be nearly steady-state, so that it has spatial weights for the displacement and the velocity, but the acceleration is modelled by a random walk with a time-varying variance. All the time varying coefficients are estimated using Kalman filtering, and the optimization problem is regularized with the spatial sum of the transient strain rate field. The authors first applied the NSF to a synthetic dataset and obtained a good recovery of the transient signal although its amplitude was similar to the noise level. They then applied the NSF to the 1996 Boso slow earthquake, and could detect the transient, but with an oversmoothing in the time domain, and could not reproduced the abrupt time history. They concluded that the NSF could be used to detect coherent motions that could be good candidates for further analysis, but that the oversmoothing problem should be addressed.

Problem: Detect transient deformation signals from large-scale geodetic arrays
Before: Network Inversion Filter (NIF)
 needs to specific potential sources of deformation to detect spatially coherent transients
Method: Network Strain Filter (NSF)
 Position = Sum of secular velocity + Spatially coherent displacement field + Site-specific noise + Reference frame errors + Observation error
 Spatial displacement field = Sum of basis wavelets (Deslauriers-Dubuc of degree 3) with time-varying weights
 Estimation of the time-varying coefficients with Kalman filtering regularized with λ^2 x spatial sum of transient rate (i.e. the transient has displacement and velocity spatial weights + approximate steady-state is obtained by modelling the acceleration by a random walk with coefficient α)
After: Synthetic case: Good recovery of the transient signal with amplitude similar to the noise
 Application to the 1996 Boso slow earthquake: Detection but oversmoothing of the transient
Open questions: Detection of coherent signals that would be good candidates for further analysis
 Oversmoothing of the estimate of the transient signal needs to be tackled

Alba (2011 [2]) used hourly water level records from four tide gauges in the Juan de Fuca Straight and the Puget Sound to determine vertical displacements, uplift rates between Episodic Tremor and Slip (ETS) events, and net uplift rates between 1996 and 2011. The noise in the tide gauges data is associated with tides, and ocean and atmospheric noise on multiple timescales (a few days for storms to decades for oscillations between ocean basins), and is assumed to be coherent between each of the four tidal gauges studied. On the contrary, the uplift due to ETS events should be different at each tidal gauge. The author first removed the tides using NOAA hourly harmonic tidal predictions. She then removed the residual noise using two different methods. The first method is based on the Discrete Wavelet Transform (DWT). More precisely, the author

applied a DWT to each of the four sites studied, and to the average of the four sites. Then, for each level of the DWT decomposition, she carried out a linear regression between the detail for one site and the detail for the average of the four sites. This process gives a coefficient for each level and for each site. She then constructed a noise signal for each site by multiplying the coefficient from the linear regression by the detail of the average over the four sites, and summing for all levels. The noise signal thus obtained was then removed from the time series. The second method uses a frequency domain transfer function to remove coherent noise at certain frequencies. She then stacked multiple events to obtain an average event uplift rate, aligning the 12 ETS events using exact timing from GPS data. A difference in uplift between the two tidal gauges at Port Angeles and Port Townsend was then clearly seen in the stacked time series. Finally, the author removed the long-term uplift rate and the long-term sea level rise to obtain an average inter-event uplift rate. She found that the inter-event deformation at a site is equal and opposite to the deformation during an ETS event, suggesting that ETS events are, on average, releasing the strain accumulated between ETS events.

Wech and Creager (2011 [51]) studied the variations of slip size and periodicity of slow slip with increasing depth in the Cascadia subduction zone. They used the waveform envelope correlation and clustering (WECC) method developed in their previous work (Wech and Creager, 2008 [50]) to detect and locate tremor epicentres, and assumed that slow slip happens at the same time and location as tremor. They then divided the tremor region into four 20-km-wide strike-perpendicular bins, and found evidence of small and frequent slip on the downdip size of the tremor zone, and larger and less frequent slip on the updip size. They speculate that higher temperatures at higher depths would produce lower frictional strength and a weaker fault. Each small slip event would thus transfer stress updip to a stronger portion of the fault, with a higher stress threshold. When enough stress has been transferred, this updip portion would slip and transfer slip further updip of the fault.

Bostock *et al.* (2012 [7]) looked for low-frequency earthquakes (LFE) by computing autocorrelations of 6-second long windows for each component of 7 stations in Vancouver Island. They then classified their LFE detections into 140 families. By stacking all waveforms of a given family, they obtained an LFE template for each family. They extended their templates by adding more stations and computing cross correlations between station data and template waveforms. They used P- and S-traveltime picks to obtain an hypocentre for each LFE template and concluded that the LFEs were located on the plate boundary and that their downdip extension coincided with the seaward extrapolation of the continental Moho. By observing the polarizations of the P- and S-waveforms of the LFE templates, they computed focal mechanisms and obtained a mixture of strike slip and thrust mechanisms, corresponding to a compressive stress field consistent with thrust faulting parallel to the plate interface.

Ghosh *et al.* (2012 [15]) used multibeam-backprojection (MBBP) to detect and locate tremor with much higher resolution. They used data recorded by 8 small-aperture seismic arrays in the Olympic peninsula during the large August 2010 Episodic Tremor and Slip (ETS) event and an entire inter-ETS cycle. They observed that the tremors were located near the plate boundary, on a layer parallel to and a few kilometres above the layer of regular earthquakes. Distinct patches, tens of kilometres of dimension, were found to produce the majority of the tremor. The propagation velocity varied from 4 to 20 km/day at large time scale (days), and up to 100 km/h at small time scale (minutes). They interpreted their observations with a model made of patches of asperities surrounded by regions slipping aseismically. Propagation velocity was supposed to be slow in the asperities area, and fast outside of the asperities area.

Wei *et al.* (2012 [52]) used the Network Strain Filter (NSF) to analyze data from 54 continuous GPS stations in the Alaska subduction zone from 2007 to 2011. They assumed that the displacement observed at a GPS station is the sum of the secular velocity, a transient field, site-specific noise, seasonal variations, reference frame errors, and observation errors. They observed an increase in the velocity rate starting at the beginning of 2010. They modelled the transient displacement field by the slip on a planar fault in an elastic homogeneous half-space, and concluded that the observations are consistent with an accumulated slip of magnitude Mw 6.9 in 23 months. They modelled the slab seismicity with an Epidemic Type Aftershock Sequence (ETAS) model, and observed an increase in the background seismicity rate beginning in mid-2010. However, no increase in the number of non volcanic tremor was reported in the area. They observed that there is a lack of large aftershock sequences in the depth range of the slab (30-70 km), which is an indicator of very low effective normal stress, and could be linked to the occurrence of long-duration slow slip events.

Bostock (2013 [6]) proposed a new model to explain the nature of a landward-dipping, low velocity zone (LVZ) that was detected in most subduction zones. Previous models in Cascadia interpreted the LVZ as the entire oceanic crust, an extended plate boundary, serpentized material above the plate boundary, or a fluid-rich layer in the overriding continental crust. In the new model, the LVZ is interpreted as upper oceanic crust. The upper oceanic crust is hydrated by hydrothermal circulation at the ridge. The free water is incorporated into hydrous minerals. As subduction begins, prograde metamorphic reactions release hydrous fluid in the upper oceanic crust. They stayed trapped by an impermeable upper plate boundary and the impermeable gabbroic lower oceanic crust. The high pore-fluid pressure explains the low shear wave velocity and the high Poisson's ratio. At about 45km depth, the onset of eclogitization liberates additional fluids and causes volumetric changes that break the plate boundary seal. The penetration of hydrous fluids in the mantle wedge leads to serpentization

of the mantle wedge material and erasure of the Moho's seismic contrast. By 100 km depth, the eclogitization is largely completed and the LVZ disappears.

Nowack and Bostock (2013 [31]) used a set of 140 low-frequency earthquakes (LFE) waveform templates in southern Vancouver Island as a record of empirical Green's functions. They used a regional 3D tomographic model, and inserted a low velocity zone under the plate boundary. They computed synthetic waveforms of a pulse using 3D ray-tracing for different source locations corresponding to the locations of the LFE waveforms templates. They then compared their synthetics to the data from the LFE templates, and carried out a grid search to check which values of P-wave velocity, ratio of P- and S-wave velocities and thickness of the low velocity zone gave the better fit. Their estimates of the thickness of the low velocity zone, the velocity contrast and the ratio between P- and S-wave velocities were consistent with the results from previous teleseismic studies.

Armbuster *et al.* (2014 [3]) proposed a new method to accurately locate tremor sources. They started with seismic data from two stations and computed the cross correlation of the seismic signals on 150 seconds time windows. They carried out a grid search on the polarization angles of each station and the offset time between both stations, and look for the greatest cross correlation value. They assumed that a tremor event occurred when the polarization angles and the offset times are consistent for several consecutive time windows. They extended the method for three stations, and looked for the consistency between the polarization angles and offsets found for the three possible pairs of stations, without imposing a duration criterion. Finally, they used the waveforms containing tremors from the three-stations detections to look for S-wave and P-wave at additional stations. With four S-wave detections and one P-wave detection, they were able to retrieve the location and depth of the tremor source with a 1 to 2 kilometres accuracy. They noticed that the polarization of the waveforms were consistent with a shear mechanism on the plate boundary. They also found out a similarity of pattern of the locations of the tremor sources for the three main Episodic Tremor and Slip (ETS) events for which they analyzed seismic recordings.

Idehara *et al.* (2014 [22]) studied the temporal clustering of tremor activity in major tectonic zones worldwide. They defined a tremor event as a period with continuing recorded tremor activity from a source located within the same bin of radius about 10-12 kilometres. The event duration is the half-width of the stacked envelope of the seismic waveforms for many stations. They analyzed the frequency distribution of the waiting time between two tremor events, and found a bimodal distribution. They then computed the correlation integral between event times. For waiting times smaller than a characteristic time τ_c , the correlation integral is non-Poissonian and seems to follow a power law. For waiting times larger than τ_c , the correlation integral follows a Poisson distribution. They applied a χ^2 test to verify when the correlation integral was statistically significantly different from a Poisson distribution, and defined τ_c as the longest waiting time for which the difference is statistically significant. The authors then computed the values of τ_c for each bin in different tectonic regions worldwide. They found that along dip, τ_c is decreasing with increasing depth. In Shikoku and Kii-Tokai, the along-strike heterogeneities of τ_c seem to correlate with localized seismic velocity anomalies. Moreover, there is a small correlation between τ_c and tremor duration. The authors interpreted the along-dip variations in τ_c to variations in fault strength due to thermal conditions, or to stress transfer along the plate interface. They hypothesized that along-strike variations may be due to other factors such as pore fluid pressure or the geometry of the plate interface, and that regional variations may be due to variable maturity of the plate interface.

Royer and Bostock (2014 [39]) generated low-frequency earthquake (LFE) templates in northern Cascadia using the same processing steps (network autocorrelation, waveform correlation cluster analysis and network cross correlation) as in Bostock *et al.* (2012 [7]). They identified their LFE templates as empirical Green's functions, which justifies their subsequent use in waveform inversions. They computed template locations using standard linearized inversion and double difference algorithm, and concluded that LFE templates parallel the plate boundary. They carried out a moment tensor inversion for each LFE template and found out that a majority of the focal mechanisms were consistent with shallow thrust faulting, although there is more variability in northern Washington state due to poorer station coverage and lower signal-to-noise ratio.

Thurber *et al.* (2014 [48]) compared the efficiency of linear and phase-weighted stacking for picking low-frequency earthquakes (LFEs) arrivals. Once initial templates have been identified using the cross-station method of Savard and Bostock (2013), the signal is stacked using linear or phase-weighted stacking. The author then used an iterative procedure in which, at each iteration, they cross-correlate the stack with the continuous seismic signal, detecting new LFEs. At the end of each iteration, all the LFE waveforms are stacked to produce a new template with a higher SNR. The phase-weighted stack produced faster a little more detections than the linear stack, and a final template with a much better SNR than the linear stack.

Bostock *et al.* (2015 [8]) studied the magnitudes of low-frequency earthquakes (LFE) templates below southern Vancouver Island. They computed the magnitudes from the waveforms using the ray approximation, and observed that the magnitude-frequency distribution was better represented by a power law, with a b-value (~ 6.3) much higher than what is observed for regular earthquakes. They assumed that the source pulse duration is measured by the reciprocal of the

instantaneous frequency, and observed a weak scaling between seismic moment and duration. They observed that the ratio of slip between two template waveforms is much higher than the ratio of pulse duration (7.36 and 1.29), and concluded that there is no self-similarity for LFE and that larger moment events appear to be the result of increased slip. To reconcile the scaling between magnitude and frequency, and the scaling between seismic moment and slip, they proposed that multiple independently slipping sources are present within the same LFE template. The scaling of LFE would thus be different from both large scale slow slip events (SSE) and regular earthquakes.

Houston (2015 [18]) studied the sensitivity of tremor to tidal stress. She divided tremor into two groups: tremors arriving before 1.5 days after the tremor front, and tremors arriving after 1.5 days after the tremor front. She computed the evolution of tidal stress within the tremor region, and computed for each point in the regional grid the ratio of tremors occurring at a given level of tidal stress divided by the total number of tremors recorded at this grid point. She noticed a much stronger correlation between tremor activity and tidal stress changes after the passage of the tremor front. She interpreted this phenomenon with a stress threshold failure model. There is a big stress increase on the fault with the arrival of the tremor front, such that the stress stays much higher than the fault strength even when the tidal stress varies. It generates a lot of tremor, but a weak influence of tides on tremor activity. After the passage of the tremor front, tides cause small variations of stress on a weaker fault, such that there is an alternance of states with fault strength higher than stress on fault, and fault strength lower than stress on fault with each tidal cycle. Thus, there are less tremors, but a stronger influence of tides on tremor activity.

Hyndman *et al.* (2015 [19]) investigated the processes that control the position of Episodic Tremor and Slip (ETS) in the Cascadia subduction zone. They noticed that the high temperatures in the young subducting oceanic plate, the geodetic data, and the recordings of coseismic subsidence in buried coastal marshes during past great earthquakes, all point out to a downdip limit of the seismogenic zone located offshore. The position of the slow slip and the tremor is well known, although the depths have some uncertainty. The slip may extend seaward of the tremor, but there is a clear separation between the seismogenic zone and the ETS zone, with the ETS zone being located about 70 km east of the downdip of the seismogenic zone, and the volcanic arc being located about 100 km east of the ETS zone. A previous study showed that the position of the subduction zone ETS does not coincide with a specific temperature or dehydration reaction. The authors pointed out that ETS has been related to high pore fluid pressures close to the plate boundary. They argued that the bending of the subducting plate at the ocean trench may introduce a large amount of water in the upper oceanic mantle, resulting in extensive serpentinization. Moreover, the serpentinization of the fore-arc mantle corner may increase its vertical impermeability, while keeping a high permeability parallel to the fault, thus channelling all the fluid updip in the subducting oceanic crust. The dehydration of the serpentinite from the upper oceanic mantle, and the focusing of rising fluids along the plate boundary should result in large amounts of fluids available at the fore-arc mantle corner. Additionally, there seems to be a good coincidence between the location of the fore-arc mantle corner, and the location of ETS. The authors then observed that the deep fore-arc crust has a very low Poisson's ratio (less than 0.22), and that the only mineral with a very low Poisson's ratio is quartz (about 0.1), which led them to conclude that there may be a significant amount of quartz (about 10 % in volume) in the deep fore-arc crust above the fore-arc mantle. Moreover, as the solubility of silica increases with temperature, fluids generated at depth and rising up the subduction channel should be rich in silica. The authors concluded that there may be a relation between quartz veins formation in the deep fore-arc crust and ETS. However, several constraints as the magnitude and mechanism of the low-frequency earthquakes, and the vertical extent of the tremor should be explained.

Plourde *et al.* (2015 [36]) have detected low-frequency earthquakes (LFEs) in Northern California during the April 2008 Episodic Tremor and Slip (ETS) event using seismic data from the EarthScope Flexible Array Mendocino Experiment (FAME). They used a combination of autodetection methods and visual identification to obtain the initial templates. Then, they recovered higher signal-to-noise (SNR) LFE signals using iterative network cross correlation. They found that the LFE families were located above the plate boundary, with a large distribution of depths (28-47 km). Three additional families were found on the Maacama and Bucknell Creek faults. On these faults, LFEs tend to occur in bursts, while repeating earthquakes occur as single events or in small groups. LFEs and earthquakes have also different frequency contents. They conclude that dehydration of the mantle and further upward migration of water through the deep crustal fault system could explain the generation of both tremor and regular seismicity on these two faults.

Frank *et al.* (2016 [13]) carried out a statistical analysis of a catalog of low-frequency earthquakes (LFEs) recorded between January 2005 and April 2007 in the Guerrero, Mexico, subduction zone. There are two sources of LFEs: in the “transient zone”, most of the LFEs occur in bursts during slow slip events, while the LFE activity is much lower during inter-slow slip periods ; in the “sweet spot”, bursts of LFEs are emitted nearly continuously. The authors translated the catalog for each LFE family into a discrete time series by binning each cataloged event into the one-minute-long time step in which it is observed. They then computed the autocorrelation sequence and the spectral density function of the time series for two 4-month-long windows, one corresponding to an inter-slow slip period, and one corresponding to the 2006 slow slip event. They observed that in the transient zone, LFEs behave as an homogeneous Poisson's process during the inter-slow slip period, and as a long memory process during the co-slow slip period. They then computed the slope of the logarithm of the spectral density function for ten-day-long sliding windows over the whole catalog. For the transient zone,

they observed an increase in the slope for each geodetically detected slow slip event. For the sweet spot, the slope stay higher than zero between geodetically detected slow slip events, implying that there may be smaller slow slip events that have yet to be observed. Moreover, the authors computed the cross correlation between the event count time series for each LFE family. They noted that there is a strong correlation in the sweet spot all the time, but that in the transition zone, the interaction is weak during the inter-slow slip period, and strong during the co-slow slip period. Finally, the authors designed a simple interaction model where the event rate at each asperity is modeled by an homogeneous Poisson's process. The time between two events is then modified by two phenomena: first, a migrating pulse decreases the inter-event time when it reaches the asperity ; second, the inter-event time decreases when an event occurs at a nearby asperity. They observed that a migrating pulse alone cannot reproduce the slope of the spectral density function, but that a high enough asperity density can reproduce the slope. They concluded that asperities at the plate interface may be locked during the inter-slow slip period, and that a new mechanism such as migrating pore pressure pulses may occur during slow slip, and activate the asperities.

Gomberg *et al.* (2016 [17]) studied the relationship between seismic moment and duration for fast and slow earthquakes population. They used GPS data and tremor catalogs in Japan and Cascadia for slow slip events, and crustal earthquakes from the SRCMOD database for fast slip events. They distinguished between unbounded events, for which fault growth is two-dimensional and moment is proportional to the cube of duration, and bounded events, for which fault growth is one dimensional and moment is proportional to duration. The proposed dislocation model does not require different scaling between fast and slow earthquakes. Instead, there is a continuous but bimodal distribution of slip modes: elastic, velocity-weakening patches generate fast slip, while viscous, velocity-strengthening background generates slow, aseismic slip. The size and distribution of patches on a fault determinate the dominant mode.

Chestler and Creager (2017 [9]) gathered a catalog of low-frequency earthquakes (LFEs) in the Olympic Peninsula, Washington. They used data from the Array of Arrays (AofA) and the Cascadia Arrays for Earthscope (CAFE) experiments, and stacked the seismograms over stations and arrays to obtain a signal with high signal-to-noise ratio (SNR). They used the peaks in the signal as potential times for LFE occurrence, and stacked the autocorrelation signals to verify the repetition in time of potential LFEs. They then inverted for the seismic moment of the LFEs using the time integral of the displacement pulse for the north and east channels, and by computing the moment rate from the displacement amplitude history. They thus gathered a catalog of 34,264 LFEs from 43 families. By analyzing the moment-frequency distribution of the LFEs, they observed that an exponential law better fitted the data than a power law, and concluded that the seismic moment of LFEs is scale-limited, either by the amount of slip, either by the area of slip. They proposed two end member rupture models: in the first one, the same unique patch slips all the time; in the second one, each LFE corresponds to a different subpatch that slips only once. However, they noted that to obtain a stress drop in the same range as the one obtained for slow slip models from geodetic inversions, the number of subpatches must remain low, and is unlikely to be higher than 10.

Chestler and Creager (2017 [10]).

Shelly (2017 [42]) assembled a catalog of more than one million low-frequency earthquakes (LFEs) recorded along the central San Andreas fault between 2001 and 2015. The waveform templates for the 88 LFE families were developed by Shelly and Hardebeck (2010 [45]) using cross correlations of seismograms from the High-Resolution Seismic Network (HRSN) borehole network installed in the vicinity of Parkfield, California. The best 100 LFEs were linearly stacked to form a high signal-to-noise ratio for each family. Event detection was then carried out over 15 years using a multichannel matched filter method. Two thresholds were used: the mean cross correlation coefficient across all channels must be higher than 0.16, and the sum of all cross correlation coefficients across all channels must be higher than 4.0. An increase in the LFE event rate was observed after the 2004 Parkfield earthquake. A large diversity of recurrence behaviours was observed among the LFE families, from semicontinuous to highly episodic. Particularly, two families exhibited bimodal recurrence patterns (about 3 and 6 days for the first one, and about 2 and 4 days for the second one). Fast (15 to 90 km/h) and slow (5-15 km/h) migrations of the LFEs were observed along the San Andreas fault. False detections may occur and can be eliminated by using a higher detection threshold for the cross correlation. The detection rate may vary along time due to station outage. Finally, the average cross correlation of detected events could be used for network monitoring.

Part II

Episodic Tremor and Slip (ETS)

Chapter 1

Slow slip

Slow slip on the plate boundary is inferred to happen when there is a reversal of the direction of motion at GPS stations, compared to the secular motion of the surface displacement.

The amplitude of the horizontal displacement measured by the GPS stations at the surface is a few millimetres. Dragert *et al.* (2001 [11]) found displacements ranging from 2 to 4 millimetres. Dragert *et al.* (2004 [12]) found an average displacement of 5 millimetres. Szeliga *et al.* (2008 [46]) found a displacement consistently lower than 6 millimetres. This should be compared to a secular velocity of 5.6 millimetres per year on average, and an inter-slip velocity of 9.7 millimetres per year on average (Dragert *et al.*, 2004 [12]).

The reversal of the direction of motion is observed during a few weeks at each GPS station. Dragert *et al.* (2001 [11]) observed a reversal lasting about 6 to 15 days depending on the GPS station for the summer 1999 event. Miller *et al.* (2002 [28]) observed a reversal lasting on average 2 to 4 weeks for the eight events between 1992 and 2001. Dragert *et al.* (2004 [12]) observed reversals lasting 1 to 3 weeks. The average dislocation risetime was found to be 14 days with a maximum of about 30 days (Schmidt and Gao, 2010 [41]).

The reversal of the direction of motion does not occur at the same time for each GPS station. Dragert *et al.* (2001 [11]) observed a 35 days time lag between the beginning of the reverse displacement at the most southeastern station and beginning of the reverse displacement at the most northwestern station for the summer 1999 event. Miller *et al.* (2002 [28]) observed an average time lag of 3 weeks between the beginning of the event at the first station and the beginning of the event at the last station for the eight events between 1992 and 2001. The overall duration of an event is 2 to 7 weeks (Gao *et al.*, 2012 [14]). This corresponds to a propagation velocity along the strike of the plate boundary of about 6 kilometres per day for the summer 1999 event (Dragert *et al.*, 2001 [11]). Dragert *et al.* (2004 [12]) found a propagation velocity varying from 5 to 15 kilometres per day. Schmidt and Gao (2010 [41]) found an average propagation rate for the slip initiation of 5.9 kilometres per day, although some fault elements showed a rate as high as 17 kilometres per day.

The recurrence interval of the eight slow slip events between 1992 and 2001 was on average 14.5 months according to Miller *et al.* (2002 [28]), or between 13 and 16 months according to Dragert *et al.* (2004 [12]).

Numerical simulation of faulting in an elastic half-space have been carried out by several authors in order to retrieve the corresponding slip at the plate interface. Dragert *et al.* (2001 [11]) found a slip of about 2 centimetres between 30 and 40 kilometres depth, and a smaller slip updip of 30 kilometres for the summer 1999 event. Numerical modelling carried out by Miller *et al.* (2002, [28]) suggests that the eight events from 1992 to 2001 were evidence of a creep of a few centimetres along the plate interface at depths of 30 to 50 kilometres. Dragert *et al.* (2004 [12]) found a slip of 2 to 4 centimetres on the plate interface bounded by the 25 and 45 kilometres depth contours. Melbourne *et al.* (2005 [27]) found a maximum slip of 3.8 centimetres centered at 28 kilometres depth with most of the slip located above 38 kilometres depth. Szeliga *et al.* (2008 [46]) found an average slip of 2 to 3 centimetres. The total area where this reversal of the direction of motion was observed was about 50 * 300 kilometres for the summer 1999 event (Dragert *et al.*, 2001 [11]). Dragert *et al.* (2001 [11]) found that the surface displacement was largest at the sites located more than 100 kilometres landward of the locked zone. Wech and Creager (2008 [50]) observed that the western boundary of the area where reversal of the direction of motion occurs is located 75 km east of the downdip edge of the seismogenic zone. The strain release from slow slip was not uniform along strike, and the greater amount of slip is centered around Port Angeles (Schmidt and Gao, 2010 [41]).

These values of slip and area correspond to earthquakes of moment magnitude 6.7 for the summer 1999 event (Dragert *et al.*, 2001 [11]), 6.8 for the July 1998 event, 6.7 for the August 1999 event, 6.7 for the December 2000 event, 6.5 for the February 2002 event (Dragert *et al.*, 2004 [12]), 6.6 for the February 2003 event (Melbourne *et al.*, 2005 [27]), 6.3 to 6.8 for

the events studied by Szeliga *et al.* (2008 [46]), and 6.1 to 6.7 for the events studied by Schmidt and Gao (2010 [41]).

The average stress drop is about 0.01 to 0.10 MPa (Schmidt and Gao, 2010 [41]).

Chapter 2

Tremor

The predominant frequency of tremors ranges from 1 to 10 Hz and is lower than that of ordinary earthquakes of similar size (10 to 20 Hz). The envelopes of tremors have gradual rise times and differ from those of a normal earthquake, which has a spike-like envelope shape (Obara, 2002 [32]). The frequency content is mainly between 1 and 5 Hz, whereas most of the energy in small earthquakes is above 10 Hz. A tremor onset is usually emergent and the signal consists of pulses of energy, often about a minute in duration. A continuous signal may last from a few minutes to several days (Rogers and Dragert, 2003 [38]).

It is only when a number of seismograph signals are viewed together that the similarity in the envelope of the seismic signal at each site identifies the signal as ETS (Rogers and Dragert, 2003 [38])

Characteristics: low amplitude, lack of energy at high frequency, emergent onsets, absence of clear impulsive phases (La Rocca *et al.*, 2009)

Depth = 30 km, near the Mohorovičić discontinuity (southwest Japan, Obara, 2002 [32]). 20 to 40 km (Rogers and Dragert, 2003 [38]).

correlate temporally and spatially with six deep slip events that have occurred over the past 7 years (Rogers and Dragert, 2003 [38])

Spatially clustered (Obara *et al.*, 2004). Belt-like distribution Patches tens kilometers of dimension (Ghosh *et al*, 2012). small-amplitude tremors that lasted from a few minutes to a few days (Obara, 2002 [32]). 1 min (Rogers and Dragert, 2003)

Duration of tremor activity = 10 to 20 days in any one region (Rogers and Dragert, 2003 [38]). Several days to a few weeks (Obara *et al.*, 2004)

Frequency = rom 1 to 10 Hz (Obara, 2002 [32]). Time windows of 35 to 50 min. 1-8 Hz (Ide *et al*, 2007) The frequency content is mainly between 1 and 5 Hz, whereas most of the energy in small earthquakes is above 10 Hz (Rogers and Dragert, 2003 [38]).

Propagation = along strike 5 to 15 km / day (Rogers and Dragert, 2003 [38]). Along-strike 5-17 km / day (Shelly *et al.*, 2007)

Short-trem 15 km up-dip in 20 min (Nankai, Shelly *et al.*, 2007) = 45 km / h

Recurrence interval = 2 to 3 months (eastern Shikoku)

Propagated with a velocity of 4 km/s, that is the source of the tremors was located at a deep portion and the envelopes were propagated by S-wave velocity (Obara, 2002 [32]).

no impulsive body wave arrivals → Difficult to locate

Chapter 3

LFEs

Depth = 30-35 km (nankai, Ide *et al.*, 2007), 7km above regular intraplate earthquakes

Location = spatially clustered, at the plate boundary, 25 to 37 km depth plate boundary contour, between two bands of seismicity (crustal and intraslab earthquakes)

Magnitude= ≥ 2

Mechanism = shear slip on low-angle thrust fault. Point-source, double-couple excitation ; combination of strike-slip and thrust faulting (Bostosck *et al.*, 2012)

Frequency = 1-10 Hz 1-8 Hz (Ide et al, 2007)

Chapter 4

Slow earthquakes

Moment / duration : $M_0 = T \times 10^{12-13}$ (slow) versus $M_0 = T^3 \times 10^{15-16}$ (regular)

Moment rate / frequency : $\dot{M}_0 \propto f^{-1}$ (slow) versus $\dot{M}_0 \propto f^{-2}$ (regular)

Chapter 5

Subduction

Plate convergence (Juan de Fuca) = 4 cm / year Age 10 million year

up-dip of 45km depth, earthquakes below the reflector (serpentinite dehydration of the mantle), down-dip within subducted crust (basalt-to-eclogite transformation) (Preston *et al.*, 2003) down to 60 km depth

Physical mechanism intraslab earthquakes: dehydration embrittlement, metamorphic dehydration (prograde metamorphism)

Low velocity layer = 3-4km thin, Vs=2-3 km/s Poisson's ratio = 0.4, depth 20-40 km (Nowack and Bostock, 2013).

Part III

Methods

Chapter 6

Time lags

6.1 Computing the amplitudes of the direct and reflected P-, SV- and SH-waves

6.1.1 Computation of the initial amplitudes at the tremor source

We denote (x, y) the coordinates of the receiver array, (x_0, y_0) the coordinates of the tremor source, d the depth of the tremor source, and β the angle between the east direction and the tremor source - receiver direction. In the $(\vec{e}_X, \vec{e}_Y, \vec{e}_Z)$ coordinate system, we thus have:

$$\vec{e}_R = \begin{pmatrix} \cos \beta \\ \sin \beta \\ 0 \end{pmatrix}, \vec{e}_T = \begin{pmatrix} -\sin \beta \\ \cos \beta \\ 0 \end{pmatrix} \text{ and } \vec{e}_Z = \begin{pmatrix} 0 \\ 0 \\ 1 \end{pmatrix} \text{ with } \beta = \text{atan2}(y - y_0, x - x_0) \quad (6.1)$$

Reversely, in the $(\vec{e}_R, \vec{e}_T, \vec{e}_Z)$ coordinate system, we have:

$$\vec{e}_X = \begin{pmatrix} \cos \beta \\ -\sin \beta \\ 0 \end{pmatrix}, \vec{e}_Y = \begin{pmatrix} \sin \beta \\ \cos \beta \\ 0 \end{pmatrix} \text{ and } \vec{e}_Z = \begin{pmatrix} 0 \\ 0 \\ 1 \end{pmatrix} \quad (6.2)$$

We denote α the angle between the vertical and the direction of propagation. In the $(\vec{e}_R, \vec{e}_T, \vec{e}_Z)$ coordinate system, we have for the direct wave:

$$\vec{e}_P = \begin{pmatrix} \sin \alpha \\ 0 \\ \cos \alpha \end{pmatrix}, \vec{e}_{SV} = \begin{pmatrix} \cos \alpha \\ 0 \\ -\sin \alpha \end{pmatrix} \text{ and } \vec{e}_{SH} = \begin{pmatrix} 0 \\ 1 \\ 0 \end{pmatrix} \text{ with } \alpha = \text{atan2}\left((x - x_0)^2 + (y - y_0)^2, d\right) \quad (6.3)$$

For the reflected wave, we have:

$$\vec{e}_P = \begin{pmatrix} \sin \alpha \\ 0 \\ -\cos \alpha \end{pmatrix}, \vec{e}_{SV} = \begin{pmatrix} \cos \alpha \\ 0 \\ \sin \alpha \end{pmatrix} \text{ and } \vec{e}_{SH} = \begin{pmatrix} 0 \\ -1 \\ 0 \end{pmatrix} \quad (6.4)$$

where α is computed using the RayTracing code.

Reversely, in the $(\vec{e}_P, \vec{e}_{SV}, \vec{e}_{SH})$ coordinate system, we have for the direct wave:

$$\vec{e}_R = \begin{pmatrix} \sin \alpha \\ \cos \alpha \\ 0 \end{pmatrix}, \vec{e}_T = \begin{pmatrix} 0 \\ 0 \\ 1 \end{pmatrix} \text{ and } \vec{e}_Z = \begin{pmatrix} \cos \alpha \\ -\sin \alpha \\ 0 \end{pmatrix} \quad (6.5)$$

For the reflected wave, we have:

$$\vec{e}_R = \begin{pmatrix} \sin \alpha \\ \cos \alpha \\ 0 \end{pmatrix}, \vec{e}_T = \begin{pmatrix} 0 \\ 0 \\ -1 \end{pmatrix} \text{ and } \vec{e}_Z = \begin{pmatrix} -\cos \alpha \\ \sin \alpha \\ 0 \end{pmatrix} \quad (6.6)$$

We compute the seismic moment M in the $(\vec{e}_X, \vec{e}_Y, \vec{e}_Z)$ coordinate system. We have:

$$M_{ij} = u_i \nu_j + u_j \nu_i \quad (6.7)$$

with:

$$\vec{u} = \begin{pmatrix} -\cos \delta \cos \phi \\ \cos \delta \sin \phi \\ \sin \delta \end{pmatrix} \text{ and } \vec{\nu} = \begin{pmatrix} \sin \delta \cos \phi \\ -\sin \delta \sin \phi \\ \cos \delta \end{pmatrix} \quad (6.8)$$

where ϕ is the strike of the subducting plate, and δ is the dip of the subducting plate. We assume that we have reverse faulting, that is the rake λ is equal to $\frac{\pi}{2}$.

We then compute the value of M in the $(\vec{e}_P, \vec{e}_{SV}, \vec{e}_{SH})$ coordinate system. We have:

$$\begin{pmatrix} M_{RR} & M_{RT} & M_{RZ} \\ M_{TR} & M_{TT} & M_{TZ} \\ M_{ZR} & M_{ZT} & M_{ZZ} \end{pmatrix} = \begin{pmatrix} \cos \beta & \sin \beta & 0 \\ -\sin \beta & \cos \beta & 0 \\ 0 & 0 & 1 \end{pmatrix} \begin{pmatrix} M_{XX} & M_{XY} & M_{XZ} \\ M_{YX} & M_{YY} & M_{YZ} \\ M_{ZX} & M_{ZY} & M_{ZZ} \end{pmatrix} \begin{pmatrix} \cos \beta & -\sin \beta & 0 \\ \sin \beta & \cos \beta & 0 \\ 0 & 0 & 1 \end{pmatrix} \quad (6.9)$$

For the direct wave, we have:

$$\begin{pmatrix} M_{PP} & M_{PSV} & M_{PSH} \\ M_{SVP} & M_{SVSV} & M_{SVSH} \\ M_{SHP} & M_{SHSV} & M_{SHSH} \end{pmatrix} = \begin{pmatrix} \sin \alpha & 0 & \cos \alpha \\ \cos \alpha & 0 & -\sin \alpha \\ 0 & 1 & 0 \end{pmatrix} \begin{pmatrix} M_{RR} & M_{RT} & M_{RZ} \\ M_{TR} & M_{TT} & M_{TZ} \\ M_{ZR} & M_{ZT} & M_{ZZ} \end{pmatrix} \begin{pmatrix} \sin \alpha & \cos \alpha & 0 \\ 0 & 0 & 1 \\ \cos \alpha & -\sin \alpha & 0 \end{pmatrix} \quad (6.10)$$

For the reflected wave, we have:

$$\begin{pmatrix} M_{PP} & M_{PSV} & M_{PSH} \\ M_{SVP} & M_{SVSV} & M_{SVSH} \\ M_{SHP} & M_{SHSV} & M_{SHSH} \end{pmatrix} = \begin{pmatrix} \sin \alpha & 0 & -\cos \alpha \\ \cos \alpha & 0 & \sin \alpha \\ 0 & -1 & 0 \end{pmatrix} \begin{pmatrix} M_{RR} & M_{RT} & M_{RZ} \\ M_{TR} & M_{TT} & M_{TZ} \\ M_{ZR} & M_{ZT} & M_{ZZ} \end{pmatrix} \begin{pmatrix} \sin \alpha & \cos \alpha & 0 \\ 0 & 0 & -1 \\ -\cos \alpha & \sin \alpha & 0 \end{pmatrix} \quad (6.11)$$

In the $(\vec{e}_P, \vec{e}_{SV}, \vec{e}_{SH})$ coordinate system, we have:

$$\vec{\Gamma} = \begin{pmatrix} \gamma_1 \\ \gamma_2 \\ \gamma_3 \end{pmatrix} = \begin{pmatrix} 1 \\ 0 \\ 0 \end{pmatrix} \quad (6.12)$$

Thus we can get the amplitude of the seismic wave at the tremor source from the strike and the dip of the subducting plate, using Equation 9.13.1 of Pujol (2003):

$$\begin{pmatrix} A_P \\ A_{SV} \\ A_{SH} \end{pmatrix} = \begin{pmatrix} M_{PP} \\ M_{SVP} \\ M_{SHP} \end{pmatrix} \quad (6.13)$$

6.1.2 Getting the reflection, conversion and transmission coefficients

We compute the reflection, conversion and transmission coefficients at the interface between two homogeneous media, following Aki and Richards (2002, ch. 5.2).

SH-wave

We have $u_x = 0$, $u_z = 0$ and $\frac{\partial}{\partial y} = 0$. Thus the wave equations become:

$$\begin{aligned} \rho \frac{\partial^2 u_y}{\partial t^2} &= \frac{\partial \sigma_{yx}}{\partial x} + \frac{\partial \sigma_{yz}}{\partial z} \\ \sigma_{xy} &= \mu \frac{\partial u_y}{\partial x} \\ \sigma_{yz} &= \mu \frac{\partial u_y}{\partial z} \\ \sigma_{xx} = \sigma_{yy} = \sigma_{zz} = \sigma_{xz} &= 0 \end{aligned} \quad (6.14)$$

The incident SH-wave is of the form:

$$u_y(t) = \dot{S}_1 \exp(i\omega(t - p_{\beta_1}x - q_{\beta_1}z)) \quad (6.15)$$

From Snell's law, we have $\frac{\sin j_1}{\beta_1} = \frac{\sin j_2}{\beta_2}$

At $z = 0$, we have $u_y(z^+) = u_y(z^-)$, and $\sigma_{yz}(z^+) = \sigma_{yz}(z^-)$ thus:

$$\begin{aligned}\dot{S}_1 + \dot{S}_1 &= \dot{S}_2 \\ -\mu_1 i \omega q_{\beta_1} \dot{S}_1 + \mu_1 i \omega q_{\beta_1} \dot{S}_1 &= -\mu_2 i \omega q_{\beta_2} \dot{S}_2\end{aligned}\tag{6.16}$$

Therefore, using $q_{\beta_1} = \frac{\cos j_1}{\beta_1}$ and $q_{\beta_2} = \frac{\cos j_2}{\beta_2}$, we find:

$$\begin{aligned}\dot{S}_1 &= \dot{S}_1 \frac{\rho_1 \beta_1 \cos j_1 - \rho_2 \beta_2 \cos j_2}{\rho_1 \beta_1 \cos j_1 + \rho_2 \beta_2 \cos j_2} \\ \dot{S}_2 &= \dot{S}_1 \frac{2 \rho_1 \beta_1 \cos j_1}{\rho_1 \beta_1 \cos j_1 + \rho_2 \beta_2 \cos j_2}\end{aligned}\tag{6.17}$$

P-wave

We have $u_y = 0$ and $\frac{\partial}{\partial y} = 0$. Thus the wave equations become:

$$\begin{aligned}\rho \frac{\partial^2 u_x}{\partial t^2} &= \frac{\partial \sigma_{xx}}{\partial x} + \frac{\partial \sigma_{xz}}{\partial z} \\ \rho \frac{\partial^2 u_z}{\partial t^2} &= \frac{\partial \sigma_{zx}}{\partial x} + \frac{\partial \sigma_{zz}}{\partial z} \\ \sigma_{xx} &= (\lambda + 2\mu) \frac{\partial u_x}{\partial x} + \lambda \frac{\partial u_z}{\partial z} \\ \sigma_{yy} &= \lambda \left(\frac{\partial u_x}{\partial x} + \frac{\partial u_z}{\partial z} \right) \\ \sigma_{zz} &= \lambda \frac{\partial u_x}{\partial x} + (\lambda + 2\mu) \frac{\partial u_z}{\partial z} \\ \sigma_{xz} &= \mu \left(\frac{\partial u_x}{\partial z} + \frac{\partial u_z}{\partial x} \right) \\ \sigma_{xy} &= \sigma_{yz} = 0\end{aligned}\tag{6.18}$$

The incident P-wave is of the form:

$$\begin{aligned}u_x(t) &= \dot{P}_1 \sin i_1 \exp(i\omega(t - p_{\alpha_1}x - q_{\alpha_1}z)) \\ u_z(t) &= \dot{P}_1 \cos i_1 \exp(i\omega(t - p_{\alpha_1}x - q_{\alpha_1}z))\end{aligned}\tag{6.19}$$

From Snell's law, we have $\frac{\sin i_1}{\alpha_1} = \frac{\sin i_2}{\alpha_2} = \frac{\sin j_1}{\beta_1} = \frac{\sin j_2}{\beta_2}$

At $z = 0$, we have $u_x(z^+) = u_x(z^-)$, $u_z(z^+) = u_z(z^-)$, $\sigma_{xz}(z^+) = \sigma_{xz}(z^-)$ and $\sigma_{zz}(z^+) = \sigma_{zz}(z^-)$ thus:

$$\begin{aligned}\dot{P}_1 \sin i_1 + \dot{P}_1 \sin i_1 + \dot{S}_1 \cos j_1 &= \dot{P}_2 \sin i_2 + \dot{S}_2 \cos j_2 \\ -\dot{P}_1 \cos i_1 + \dot{P}_1 \cos i_1 - \dot{S}_1 \sin j_1 &= -\dot{P}_2 \cos i_2 + \dot{S}_2 \sin j_2 \\ \mu_1(-q_{\alpha_1} \dot{P}_1 \sin i_1 + q_{\alpha_1} \dot{P}_1 \sin i_1 + q_{\beta_1} \dot{S}_1 \cos j_1) + \mu_1(-p_{\alpha_1} \dot{P}_1 \cos i_1 + p_{\alpha_1} \dot{P}_1 \cos i_1 - p_{\beta_1} \dot{S}_1 \sin j_1) &= \\ \mu_2(-q_{\alpha_2} \dot{P}_2 \sin i_2 - q_{\beta_2} \dot{S}_2 \cos j_2) + \mu_2(-p_{\alpha_2} \dot{P}_2 \cos i_2 + p_{\beta_2} \dot{S}_2 \sin j_2) &= \\ \lambda_1(p_{\alpha_1} \dot{P}_1 \sin i_1 + p_{\alpha_1} \dot{P}_1 \sin i_1 + p_{\beta_1} \dot{S}_1 \cos j_1) + (\lambda_1 + 2\mu_1)(q_{\alpha_1} \dot{P}_1 \cos i_1 + q_{\alpha_1} \dot{P}_1 \cos i_1 - q_{\beta_1} \dot{S}_1 \sin j_1) &= \\ \lambda_2(p_{\alpha_2} \dot{P}_2 \sin i_2 + p_{\beta_2} \dot{S}_2 \cos j_2) + (\lambda_2 + 2\mu_2)(q_{\alpha_2} \dot{P}_2 \cos i_2 - q_{\beta_2} \dot{S}_2 \sin j_2) &=\end{aligned}\tag{6.20}$$

that is:

$$\begin{aligned}-\dot{P}_2 \sin i_2 - \dot{S}_2 \cos j_2 + \dot{P}_1 \sin i_1 + \dot{S}_1 \cos j_1 &= -\dot{P}_1 \sin i_1 \\ \dot{P}_2 \cos i_2 - \dot{S}_2 \sin j_2 + \dot{P}_1 \cos i_1 - \dot{S}_1 \sin j_1 &= \dot{P}_1 \cos i_1 \\ \mu_2 q_{\alpha_2} \dot{P}_2 \sin i_2 + \mu_2 p_{\alpha_2} \dot{P}_2 \cos i_2 + \mu_2 q_{\beta_2} \dot{S}_2 \cos j_2 - \mu_2 p_{\beta_2} \dot{S}_2 \sin j_2 &= \\ + \mu_1 q_{\alpha_1} \dot{P}_1 \sin i_1 + \mu_1 p_{\alpha_1} \dot{P}_1 \cos i_1 + \mu_1 q_{\beta_1} \dot{S}_1 \cos j_1 - \mu_1 p_{\beta_1} \dot{S}_1 \sin j_1 &= \\ \mu_1 q_{\alpha_1} \dot{P}_1 \sin i_1 + \mu_1 p_{\alpha_1} \dot{P}_1 \cos i_1 &= \\ -\lambda_2 p_{\alpha_2} \dot{P}_2 \sin i_2 - (\lambda_2 + 2\mu_2) q_{\alpha_2} \dot{P}_2 \cos i_2 - \lambda_2 p_{\beta_2} \dot{S}_2 \cos j_2 + (\lambda_2 + 2\mu_2) q_{\beta_2} \dot{S}_2 \sin j_2 &= \\ + \lambda_1 p_{\alpha_1} \dot{P}_1 \sin i_1 + (\lambda_1 + 2\mu_1) q_{\alpha_1} \dot{P}_1 \cos i_1 + \lambda_1 p_{\beta_1} \dot{S}_1 \cos j_1 - (\lambda_1 + 2\mu_1) q_{\beta_1} \dot{S}_1 \sin j_1 &= \\ -\lambda_1 p_{\alpha_1} \dot{P}_1 \sin i_1 - (\lambda_1 + 2\mu_1) q_{\alpha_1} \dot{P}_1 \cos i_1 &=\end{aligned}\tag{6.21}$$

that is:

$$\begin{aligned}
-\dot{P}_2 \sin i_2 - \dot{S}_2 \cos j_2 + \dot{P}_1 \sin i_1 + \dot{S}_1 \cos j_1 &= -\dot{P}_1 \sin i_1 \\
\dot{P}_2 \cos i_2 - \dot{S}_2 \sin j_2 + \dot{P}_1 \cos i_1 - \dot{S}_1 \sin j_1 &= \dot{P}_1 \cos i_1 \\
(\mu_2 q_{\alpha_2} \sin i_2 + \mu_2 p_{\alpha_2} \cos i_2) \dot{P}_2 + (\mu_2 q_{\beta_2} \cos j_2 - \mu_2 p_{\beta_2} \sin j_2) \dot{S}_2 \\
+ (\mu_1 q_{\alpha_1} \sin i_1 + \mu_1 p_{\alpha_1} \cos i_1) \dot{P}_1 + (\mu_1 q_{\beta_1} \cos j_1 - \mu_1 p_{\beta_1} \sin j_1) \dot{S}_1 &= \\
(\mu_1 q_{\alpha_1} \sin i_1 + \mu_1 p_{\alpha_1} \cos i_1) \dot{P}_1 \\
-(\lambda_2 p_{\alpha_2} \sin i_2 + (\lambda_2 + 2\mu_2) q_{\alpha_2} \cos i_2) \dot{P}_2 - (\lambda_2 p_{\beta_2} \cos j_2 - (\lambda_2 + 2\mu_2) q_{\beta_2} \sin j_2) \dot{S}_2 \\
+(\lambda_1 p_{\alpha_1} \sin i_1 + (\lambda_1 + 2\mu_1) q_{\alpha_1} \cos i_1) \dot{P}_1 + (\lambda_1 p_{\beta_1} \cos j_1 - (\lambda_1 + 2\mu_1) q_{\beta_1} \sin j_1) \dot{S}_1 &= \\
-(\lambda_1 p_{\alpha_1} \sin i_1 + (\lambda_1 + 2\mu_1) q_{\alpha_1} \cos i_1) \dot{P}_1
\end{aligned} \tag{6.22}$$

that is:

$$\begin{aligned}
-\alpha_2 p_{\alpha_2} \dot{P}_2 - \cos j_2 \dot{S}_2 + \alpha_1 p_{\alpha_1} \dot{P}_1 + \cos j_1 \dot{S}_1 &= -\alpha_1 p_{\alpha_1} \dot{P}_1 \\
\cos i_2 \dot{P}_2 - \beta_2 p_{\beta_2} \dot{S}_2 + \cos i_1 \dot{P}_1 - \beta_1 p_{\beta_1} \dot{S}_1 &= \cos i_1 \dot{P}_1 \\
(2\rho_2 \beta_2^2 p_{\alpha_2} \cos i_2) \dot{P}_2 + \rho_2 \beta_2 (1 - 2\beta_2^2 p_{\beta_2}^2) \dot{S}_2 \\
+(2\rho_1 \beta_1^2 p_{\alpha_1} \cos i_1) \dot{P}_1 + \rho_1 \beta_1 (1 - 2\beta_1^2 p_{\beta_1}^2) \dot{S}_1 &= \\
(2\rho_1 \beta_1^2 p_{\alpha_1} \cos i_1) \dot{P}_1 \\
-\rho_2 \alpha_2 (1 - 2\beta_2^2 p_{\alpha_2}^2) \dot{P}_2 + 2\rho_2 \beta_2^2 p_{\beta_2} \cos j_2 \dot{S}_2 \\
+\rho_1 \alpha_1 (1 - 2\beta_1^2 p_{\alpha_1}^2) \dot{P}_1 - 2\rho_1 \beta_1^2 p_{\beta_1} \cos j_1 \dot{S}_1 &= \\
-\rho_1 \alpha_1 (1 - 2\beta_1^2 p_{\alpha_1}^2) \dot{P}_1
\end{aligned} \tag{6.23}$$

that is:

$$M \begin{pmatrix} \dot{P}_2 \\ \dot{S}_2 \\ \dot{P}_1 \\ \dot{S}_1 \end{pmatrix} = N \begin{pmatrix} 0 \\ 0 \\ 0 \\ \dot{P}_1 \end{pmatrix} \tag{6.24}$$

with:

$$M = \begin{pmatrix} -\alpha_2 p_{\alpha_2} & -\cos j_2 & \alpha_1 p_{\alpha_1} & \cos j_1 \\ \cos i_2 & -\beta_2 p_{\beta_2} & \cos i_1 & -\beta_1 p_{\beta_1} \\ 2\rho_2 \beta_2^2 p_{\alpha_2} \cos i_2 & \rho_2 \beta_2 (1 - 2\beta_2^2 p_{\beta_2}^2) & 2\rho_1 \beta_1^2 p_{\alpha_1} \cos i_1 & \rho_1 \beta_1 (1 - 2\beta_1^2 p_{\beta_1}^2) \\ -\rho_2 \alpha_2 (1 - 2\beta_2^2 p_{\alpha_2}^2) & 2\rho_2 \beta_2^2 p_{\beta_2} \cos j_2 & \rho_1 \alpha_1 (1 - 2\beta_1^2 p_{\alpha_1}^2) & -2\rho_1 \beta_1^2 p_{\beta_1} \cos j_1 \end{pmatrix} \tag{6.25}$$

and:

$$N = \begin{pmatrix} 0 & 0 & -\alpha_1 p_{\alpha_1} & 0 \\ 0 & 0 & \cos i_1 & 0 \\ 0 & 0 & 2\rho_1 \beta_1^2 p_{\alpha_1} \cos i_1 & 0 \\ 0 & 0 & -\rho_1 \alpha_1 (1 - 2\beta_1^2 p_{\alpha_1}^2) & 0 \end{pmatrix} \tag{6.26}$$

SV-wave

We have $u_y = 0$ and $\frac{\partial}{\partial y} = 0$. Thus the wave equations become:

$$\begin{aligned}
\rho \frac{\partial^2 u_x}{\partial t^2} &= \frac{\partial \sigma_{xx}}{\partial x} + \frac{\partial \sigma_{xz}}{\partial z} \\
\rho \frac{\partial^2 u_z}{\partial t^2} &= \frac{\partial \sigma_{zx}}{\partial x} + \frac{\partial \sigma_{zz}}{\partial z} \\
\sigma_{xx} &= (\lambda + 2\mu) \frac{\partial u_x}{\partial x} + \lambda \frac{\partial u_z}{\partial z} \\
\sigma_{yy} &= \lambda \left(\frac{\partial u_x}{\partial x} + \frac{\partial u_z}{\partial z} \right) \\
\sigma_{zz} &= \lambda \frac{\partial u_x}{\partial x} + (\lambda + 2\mu) \frac{\partial u_z}{\partial z} \\
\sigma_{xz} &= \mu \left(\frac{\partial u_x}{\partial z} + \frac{\partial u_z}{\partial x} \right) \\
\sigma_{xy} &= \sigma_{yz} = 0
\end{aligned} \tag{6.27}$$

The incident S-wave is of the form:

$$\begin{aligned}
u_x(t) &= \dot{S}_1 \cos j_1 \exp(i\omega(t - p_{\beta_1}x - q_{\beta_1}z)) \\
u_z(t) &= -\dot{S}_1 \sin j_1 \exp(i\omega(t - p_{\beta_1}x - q_{\beta_1}z))
\end{aligned} \tag{6.28}$$

From Snell's law, we have $\frac{\sin i_1}{\alpha_1} = \frac{\sin i_2}{\alpha_2} = \frac{\sin j_1}{\beta_1} = \frac{\sin j_2}{\beta_2}$

At $z = 0$, we have $u_x(z^+) = u_x(z^-)$, $u_z(z^+) = u_z(z^-)$, $\sigma_{xz}(z^+) = \sigma_{xz}(z^-)$ and $\sigma_{zz}(z^+) = \sigma_{zz}(z^-)$ thus:

$$\begin{aligned}
&\dot{S}_1 \cos j_1 + \dot{P}_1 \sin i_1 + \dot{S}_1 \cos j_1 = \dot{P}_2 \sin i_2 + \dot{S}_2 \cos j_2 \\
&\dot{S}_1 \sin j_1 + \dot{P}_1 \cos i_1 - \dot{S}_1 \sin j_1 = -\dot{P}_2 \cos i_2 + \dot{S}_2 \sin j_2 \\
&\mu_1(-q_{\beta_1} \dot{S}_1 \cos j_1 + q_{\alpha_1} \dot{P}_1 \sin i_1 + q_{\beta_1} \dot{S}_1 \cos j_1) + \mu_1(p_{\beta_1} \dot{S}_1 \sin j_1 + p_{\alpha_1} \dot{P}_1 \cos i_1 - p_{\beta_1} \dot{S}_1 \sin j_1) = \\
&\quad \mu_2(-q_{\alpha_2} \dot{P}_2 \sin i_2 - q_{\beta_2} \dot{S}_2 \cos j_2) + \mu_2(-p_{\alpha_2} \dot{P}_2 \cos i_2 + p_{\beta_2} \dot{S}_2 \sin j_2) \\
&\lambda_1(p_{\beta_1} \dot{S}_1 \cos j_1 + p_{\alpha_1} \dot{P}_1 \sin i_1 + p_{\beta_1} \dot{S}_1 \cos j_1) + (\lambda_1 + 2\mu_1)(-q_{\beta_1} \dot{S}_1 \sin j_1 + q_{\alpha_1} \dot{P}_1 \cos i_1 - q_{\beta_1} \dot{S}_1 \sin j_1) = \\
&\quad \lambda_2(p_{\alpha_2} \dot{P}_2 \sin i_2 + p_{\beta_2} \dot{S}_2 \cos j_2) + (\lambda_2 + 2\mu_2)(q_{\alpha_2} \dot{P}_2 \cos i_2 - q_{\beta_2} \dot{S}_2 \sin j_2)
\end{aligned} \tag{6.29}$$

that is:

$$\begin{aligned}
&-\dot{P}_2 \sin i_2 - \dot{S}_2 \cos j_2 + \dot{P}_1 \sin i_1 + \dot{S}_1 \cos j_1 = -\dot{S}_1 \cos j_1 \\
&\dot{P}_2 \cos i_2 - \dot{S}_2 \sin j_2 + \dot{P}_1 \cos i_1 - \dot{S}_1 \sin j_1 = -\dot{S}_1 \sin j_1 \\
&\mu_2 q_{\alpha_2} \dot{P}_2 \sin i_2 + \mu_2 p_{\alpha_2} \dot{P}_2 \cos i_2 + \mu_2 q_{\beta_2} \dot{S}_2 \cos j_2 - \mu_2 p_{\beta_2} \dot{S}_2 \sin j_2 \\
&+ \mu_1 q_{\alpha_1} \dot{P}_1 \sin i_1 + \mu_1 p_{\alpha_1} \dot{P}_1 \cos i_1 + \mu_1 q_{\beta_1} \dot{S}_1 \cos j_1 - \mu_1 p_{\beta_1} \dot{S}_1 \sin j_1 = \\
&\quad \mu_1 q_{\beta_1} \dot{S}_1 \cos j_1 - \mu_1 p_{\beta_1} \dot{S}_1 \sin j_1 \\
&-\lambda_2 p_{\alpha_2} \dot{P}_2 \sin i_2 - (\lambda_2 + 2\mu_2) q_{\alpha_2} \dot{P}_2 \cos i_2 - \lambda_2 p_{\beta_2} \dot{S}_2 \cos j_2 + (\lambda_2 + 2\mu_2) q_{\beta_2} \dot{S}_2 \sin j_2 \\
&+ \lambda_1 p_{\alpha_1} \dot{P}_1 \sin i_1 + (\lambda_1 + 2\mu_1) q_{\alpha_1} \dot{P}_1 \cos i_1 + \lambda_1 p_{\beta_1} \dot{S}_1 \cos j_1 - (\lambda_1 + 2\mu_1) q_{\beta_1} \dot{S}_1 \sin j_1 = \\
&\quad -\lambda_1 p_{\beta_1} \dot{S}_1 \cos j_1 + (\lambda_1 + 2\mu_1) q_{\beta_1} \dot{S}_1 \sin j_1
\end{aligned} \tag{6.30}$$

that is:

$$\begin{aligned}
&-\dot{P}_2 \sin i_2 - \dot{S}_2 \cos j_2 + \dot{P}_1 \sin i_1 + \dot{S}_1 \cos j_1 = -\dot{S}_1 \cos j_1 \\
&\dot{P}_2 \cos i_2 - \dot{S}_2 \sin j_2 + \dot{P}_1 \cos i_1 - \dot{S}_1 \sin j_1 = -\dot{S}_1 \sin j_1 \\
&(\mu_2 q_{\alpha_2} \sin i_2 + \mu_2 p_{\alpha_2} \cos i_2) \dot{P}_2 + (\mu_2 q_{\beta_2} \cos j_2 - \mu_2 p_{\beta_2} \sin j_2) \dot{S}_2 \\
&+ (\mu_1 q_{\alpha_1} \sin i_1 + \mu_1 p_{\alpha_1} \cos i_1) \dot{P}_1 + (\mu_1 q_{\beta_1} \cos j_1 - \mu_1 p_{\beta_1} \sin j_1) \dot{S}_1 = \\
&\quad (\mu_1 q_{\beta_1} \cos j_1 - \mu_1 p_{\beta_1} \sin j_1) \dot{S}_1 \\
&-(\lambda_2 p_{\alpha_2} \sin i_2 + (\lambda_2 + 2\mu_2) q_{\alpha_2} \cos i_2) \dot{P}_2 - (\lambda_2 p_{\beta_2} \cos j_2 - (\lambda_2 + 2\mu_2) q_{\beta_2} \sin j_2) \dot{S}_2 \\
&+ (\lambda_1 p_{\alpha_1} \sin i_1 + (\lambda_1 + 2\mu_1) q_{\alpha_1} \cos i_1) \dot{P}_1 + (\lambda_1 p_{\beta_1} \cos j_1 - (\lambda_1 + 2\mu_1) q_{\beta_1} \sin j_1) \dot{S}_1 = \\
&\quad (-\lambda_1 p_{\beta_1} \cos j_1 + (\lambda_1 + 2\mu_1) q_{\beta_1} \sin j_1) \dot{S}_1
\end{aligned} \tag{6.31}$$

that is:

$$\begin{aligned}
-\alpha_2 p_{\alpha_2} \dot{P}_2 - \cos j_2 \dot{S}_2 + \alpha_1 p_{\alpha_1} \dot{P}_1 + \cos j_1 \dot{S}_1 &= -\cos j_1 \dot{S}_1 \\
\cos i_2 \dot{P}_2 - \beta_2 p_{\beta_2} \dot{S}_2 + \cos i_1 \dot{P}_1 - \beta_1 p_{\beta_1} \dot{S}_1 &= -\beta_1 p_{\beta_1} \dot{S}_1 \\
(2\rho_2 \beta_2^2 p_{\alpha_2} \cos i_2) \dot{P}_2 + \rho_2 \beta_2 (1 - 2\beta_2^2 p_{\beta_2}^2) \dot{S}_2 & \\
+(2\rho_1 \beta_1^2 p_{\alpha_1} \cos i_1) \dot{P}_1 + \rho_1 \beta_1 (1 - 2\beta_1^2 p_{\beta_1}^2) \dot{S}_1 &= \\
\rho_1 \beta_1 (1 - 2\beta_1^2 p_{\beta_1}^2) \dot{S}_1 & \\
-\rho_2 \alpha_2 (1 - 2\beta_2^2 p_{\alpha_2}^2) \dot{P}_2 + 2\rho_2 \beta_2^2 p_{\beta_2} \cos j_2 \dot{S}_2 & \\
+\rho_1 \alpha_1 (1 - 2\beta_1^2 p_{\alpha_1}^2) \dot{P}_1 - 2\rho_1 \beta_1^2 p_{\beta_1} \cos j_1 \dot{S}_1 &= \\
2\rho_1 \beta_1^2 p_{\beta_1} \cos j_1 \dot{S}_1 &
\end{aligned} \tag{6.32}$$

that is:

$$M \begin{pmatrix} \dot{P}_2 \\ \dot{S}_2 \\ \dot{P}_1 \\ \dot{S}_1 \end{pmatrix} = N \begin{pmatrix} 0 \\ 0 \\ 0 \\ 0 \end{pmatrix} \tag{6.33}$$

with:

$$M = \begin{pmatrix} -\alpha_2 p_{\alpha_2} & -\cos j_2 & \alpha_1 p_{\alpha_1} & \cos j_1 \\ \cos i_2 & -\beta_2 p_{\beta_2} & \cos i_1 & -\beta_1 p_{\beta_1} \\ 2\rho_2 \beta_2^2 p_{\alpha_2} \cos i_2 & \rho_2 \beta_2 (1 - 2\beta_2^2 p_{\beta_2}^2) & 2\rho_1 \beta_1^2 p_{\alpha_1} \cos i_1 & \rho_1 \beta_1 (1 - 2\beta_1^2 p_{\beta_1}^2) \\ -\rho_2 \alpha_2 (1 - 2\beta_2^2 p_{\alpha_2}^2) & 2\rho_2 \beta_2^2 p_{\beta_2} \cos j_2 & \rho_1 \alpha_1 (1 - 2\beta_1^2 p_{\alpha_1}^2) & -2\rho_1 \beta_1^2 p_{\beta_1} \cos j_1 \end{pmatrix} \tag{6.34}$$

and:

$$N = \begin{pmatrix} 0 & 0 & 0 & -\cos j_1 \\ 0 & 0 & 0 & -\beta_1 p_{\beta_1} \\ 0 & 0 & 0 & \rho_1 \beta_1 (1 - 2\beta_1^2 p_{\beta_1}^2) \\ 0 & 0 & 0 & 2\rho_1 \beta_1^2 p_{\beta_1} \cos j_1 \end{pmatrix} \tag{6.35}$$

6.2 Cross-correlation of tremor recordings

6.2.1 Definitions

We define the Fourier transform \hat{f} of the function f by:

$$\hat{f}(\omega) = \frac{1}{\sqrt{2\pi}} \int_{-\infty}^{\infty} f(t) e^{-i\omega t} dt \tag{6.36}$$

$$f(t) = \frac{1}{\sqrt{2\pi}} \int_{-\infty}^{\infty} \hat{f}(\omega) e^{i\omega t} d\omega \tag{6.37}$$

We define the convolution product by:

$$(f * g)(t) = \int_{-\infty}^{\infty} f(\tau) g(t - \tau) d\tau \tag{6.38}$$

We have:

$$(\hat{f} * \hat{g})(\omega) = \sqrt{2\pi} \hat{f}(\omega) \hat{g}(\omega) \tag{6.39}$$

and:

$$(\hat{f}g)(\omega) = \frac{1}{\sqrt{2\pi}} \hat{f}(\omega) * \hat{g}(\omega) \tag{6.40}$$

We define the cross correlation by:

$$(f \otimes g)(t) = \int_{-\infty}^{\infty} f^*(\tau) g(t + \tau) d\tau \tag{6.41}$$

where f^* is the complex conjugate of f . We have:

$$(f \hat{\otimes} g)(\omega) = \sqrt{2\pi} \hat{f}^*(\omega) \hat{g}(\omega) \quad (6.42)$$

and:

$$(\hat{f}g)(\omega) = \frac{1}{\sqrt{2\pi}} \hat{f}^*(\omega) \otimes \hat{g}(\omega) \quad (6.43)$$

Finally, we have:

$$(f(t) * g(t)) \otimes (f(t) * g(t)) = (f(t) \otimes f(t)) * (g(t) \otimes g(t)) \quad (6.44)$$

If we have a point source at ξ with a source function $f_k(t)$ for $k = 1, 2, 3$, then we can express the displacement $u(x, t)$ with the Green's function:

$$u_i(x, t) = \int_{-\infty}^{\infty} G_{ik}(x, \xi, t - \tau) f_k(\xi, \tau) d\tau \quad (6.45)$$

In the case of a moment tensor, we have:

$$u_i(x, t) = \int_{-\infty}^{\infty} \frac{\partial G_{ip}}{\partial \xi_q}(x, \xi, t - \tau) M_{pq}(\xi, \tau) d\tau \quad (6.46)$$

In the Fourier domain, we have:

$$\hat{u}_i(x, \omega) = \sqrt{2\pi} \hat{G}_{ik}(x, \xi, \omega) \hat{f}_k(\xi, \omega) \quad (6.47)$$

or:

$$\hat{u}_i(x, \omega) = \sqrt{2\pi} \frac{\partial \hat{G}_{ip}}{\partial \xi_q}(x, \xi, \omega) M_{pq}(\xi, \omega) \quad (6.48)$$

When we compute the cross correlation between two components of the displacements, we have:

$$(u_i \hat{\otimes} u_j)(x, t) = \int_{-\infty}^{\infty} u_i^*(x, \tau) u_j(x, t + \tau) d\tau \quad (6.49)$$

In the Fourier domain, we have:

$$\begin{aligned} (u_i \hat{\otimes} u_j)(x, \omega) &= \sqrt{2\pi} \hat{u}_i^*(x, \omega) \hat{u}_j(x, \omega) \\ &= (2\pi)^{\frac{3}{2}} [\hat{G}_{ik}^*(x, \xi, \omega) \hat{f}_k^*(\xi, \omega)] [\hat{G}_{jl}(x, \xi, \omega) \hat{f}_l(\xi, \omega)] \\ &= (2\pi)^{\frac{3}{2}} [\frac{\partial \hat{G}_{ip}}{\partial \xi_q}^*(x, \xi, \omega) M_{pq}^*(\xi, \omega)] [\frac{\partial \hat{G}_{jr}}{\partial \xi_s}(x, \xi, \omega) M_{rs}(\xi, \omega)] \end{aligned} \quad (6.50)$$

6.2.2 Change of coordinates

Point source

Equation (15) can be written as:

$$\begin{pmatrix} (u_1 \hat{\otimes} u_1) & (u_1 \hat{\otimes} u_2) & (u_1 \hat{\otimes} u_3) \\ (u_2 \hat{\otimes} u_1) & (u_2 \hat{\otimes} u_2) & (u_2 \hat{\otimes} u_3) \\ (u_3 \hat{\otimes} u_1) & (u_3 \hat{\otimes} u_2) & (u_3 \hat{\otimes} u_3) \end{pmatrix} = (2\pi)^{\frac{3}{2}} \begin{pmatrix} \hat{G}_{11}^* & \hat{G}_{12}^* & \hat{G}_{13}^* \\ \hat{G}_{21}^* & \hat{G}_{22}^* & \hat{G}_{23}^* \\ \hat{G}_{31}^* & \hat{G}_{32}^* & \hat{G}_{33}^* \end{pmatrix} \begin{pmatrix} \hat{f}_1^* \\ \hat{f}_2^* \\ \hat{f}_3^* \end{pmatrix} (\hat{f}_1 \quad \hat{f}_2 \quad \hat{f}_3) \begin{pmatrix} \hat{G}_{11} & \hat{G}_{21} & \hat{G}_{31} \\ \hat{G}_{12} & \hat{G}_{22} & \hat{G}_{32} \\ \hat{G}_{13} & \hat{G}_{23} & \hat{G}_{33} \end{pmatrix} \quad (6.51)$$

that is:

$$\hat{U} = (2\pi)^{\frac{3}{2}} \hat{G}^* \hat{f}^* \hat{f}^T \hat{G}^T \quad (6.52)$$

We define a new coordinate system with the unit vectors $n^{(1)}$, $n^{(2)}$ and $n^{(3)}$, and the matrix N by:

$$N = \begin{pmatrix} n_1^{(1)} & n_1^{(2)} & n_1^{(3)} \\ n_2^{(1)} & n_2^{(2)} & n_2^{(3)} \\ n_3^{(1)} & n_3^{(2)} & n_3^{(3)} \end{pmatrix} \quad (6.53)$$

In the new coordinate system, the Green's function is equal to $G' = N^T G N$, thus we have:

$$N^T \hat{U} N = (2\pi)^{\frac{3}{2}} \hat{G}'^* N^T \hat{f}^* \hat{f}^T N \hat{G}'^T \quad (6.54)$$

with:

$$N^T \hat{U} N = \begin{pmatrix} (u.n^{(1)} \hat{\otimes} u.n^{(1)}) & (u.n^{(1)} \hat{\otimes} u.n^{(2)}) & (u.n^{(1)} \hat{\otimes} u.n^{(3)}) \\ (u.n^{(2)} \hat{\otimes} u.n^{(1)}) & (u.n^{(2)} \hat{\otimes} u.n^{(2)}) & (u.n^{(2)} \hat{\otimes} u.n^{(3)}) \\ (u.n^{(3)} \hat{\otimes} u.n^{(1)}) & (u.n^{(3)} \hat{\otimes} u.n^{(2)}) & (u.n^{(3)} \hat{\otimes} u.n^{(3)}) \end{pmatrix} \quad (6.55)$$

If we choose N_1 such that:

$$N_1^T \hat{f} = \begin{pmatrix} \hat{F} \\ 0 \\ 0 \end{pmatrix} \quad (6.56)$$

we get:

$$N_1^T \hat{U} N_1 = (2\pi)^{\frac{3}{2}} \hat{F}^* \hat{F} \begin{pmatrix} \hat{G}'_{11}^* \hat{G}'_{11} & \hat{G}'_{11}^* \hat{G}'_{21} & \hat{G}'_{11}^* \hat{G}'_{31} \\ \hat{G}'_{21}^* \hat{G}'_{11} & \hat{G}'_{21}^* \hat{G}'_{21} & \hat{G}'_{21}^* \hat{G}'_{31} \\ \hat{G}'_{31}^* \hat{G}'_{11} & \hat{G}'_{31}^* \hat{G}'_{21} & \hat{G}'_{31}^* \hat{G}'_{31} \end{pmatrix} \quad (6.57)$$

If we choose N_2 such that:

$$N_2^T \hat{f} = \begin{pmatrix} 0 \\ \hat{F} \\ 0 \end{pmatrix} \quad (6.58)$$

we get:

$$N_2^T \hat{U} N_2 = (2\pi)^{\frac{3}{2}} \hat{F}^* \hat{F} \begin{pmatrix} \hat{G}'_{12}^* \hat{G}'_{12} & \hat{G}'_{12}^* \hat{G}'_{22} & \hat{G}'_{12}^* \hat{G}'_{32} \\ \hat{G}'_{22}^* \hat{G}'_{12} & \hat{G}'_{22}^* \hat{G}'_{22} & \hat{G}'_{22}^* \hat{G}'_{32} \\ \hat{G}'_{32}^* \hat{G}'_{12} & \hat{G}'_{32}^* \hat{G}'_{22} & \hat{G}'_{32}^* \hat{G}'_{32} \end{pmatrix} \quad (6.59)$$

If we choose N_3 such that:

$$N_3^T \hat{f} = \begin{pmatrix} 0 \\ 0 \\ \hat{F} \end{pmatrix} \quad (6.60)$$

we get:

$$N_3^T \hat{U} N_3 = (2\pi)^{\frac{3}{2}} \hat{F}^* \hat{F} \begin{pmatrix} \hat{G}'_{13}^* \hat{G}'_{13} & \hat{G}'_{13}^* \hat{G}'_{23} & \hat{G}'_{13}^* \hat{G}'_{33} \\ \hat{G}'_{23}^* \hat{G}'_{13} & \hat{G}'_{23}^* \hat{G}'_{23} & \hat{G}'_{23}^* \hat{G}'_{33} \\ \hat{G}'_{33}^* \hat{G}'_{13} & \hat{G}'_{33}^* \hat{G}'_{23} & \hat{G}'_{33}^* \hat{G}'_{33} \end{pmatrix} \quad (6.61)$$

If we define strike ϕ , dip δ and rake λ , we can define the following vectors:

$$e_1 = \begin{pmatrix} \sin \phi \\ \cos \phi \\ 0 \end{pmatrix}, e_2 = \begin{pmatrix} \cos \phi \\ -\sin \phi \\ 0 \end{pmatrix}, e_3 = \cos \delta e_2 - \sin \delta e_z = \begin{pmatrix} \cos \phi \cos \delta \\ -\sin \phi \cos \delta \\ -\sin \delta \end{pmatrix} \text{ and } e_4 = \sin \delta e_2 + \cos \delta e_z = \begin{pmatrix} \cos \phi \sin \delta \\ -\sin \phi \sin \delta \\ \cos \delta \end{pmatrix} \quad (6.62)$$

and the new coordinate system (u, v, w) with:

$$u = \cos \lambda e_1 - \sin \lambda e_3, v = -\sin \lambda e_1 - \cos \lambda e_3 \text{ and } w = e_4 \quad (6.63)$$

Thus we have:

$$u = \begin{pmatrix} \sin \phi \cos \lambda - \cos \phi \cos \delta \sin \lambda \\ \cos \phi \cos \lambda + \sin \phi \cos \delta \sin \lambda \\ \sin \delta \sin \lambda \end{pmatrix}, v = \begin{pmatrix} -\sin \phi \sin \lambda - \cos \phi \cos \delta \cos \lambda \\ -\cos \phi \sin \lambda + \sin \phi \cos \delta \sin \lambda \\ -\sin \delta \cos \lambda \end{pmatrix} \text{ and } w = \begin{pmatrix} \cos \phi \sin \delta \\ -\sin \phi \sin \delta \\ \cos \delta \end{pmatrix} \quad (6.64)$$

We can choose:

$$N_1 = \begin{pmatrix} u_x & v_x & w_x \\ u_y & v_y & w_y \\ u_z & v_z & w_z \end{pmatrix} = \begin{pmatrix} \sin \phi \cos \lambda - \cos \phi \cos \delta \sin \lambda & -\sin \phi \sin \lambda - \cos \phi \cos \delta \cos \lambda & \cos \phi \sin \delta \\ \cos \phi \cos \lambda + \sin \phi \cos \delta \sin \lambda & -\cos \phi \sin \lambda + \sin \phi \cos \delta \sin \lambda & -\sin \phi \sin \delta \\ \sin \delta \sin \lambda & -\sin \delta \cos \lambda & \cos \delta \end{pmatrix} \quad (6.65)$$

to get Equation (19). To get Equations (21) and (23), we just have to permute the columns of N_1 to get N_2 and N_3 . If we go back into the time domain, we have:

$$N_k^T \begin{pmatrix} u_1 \otimes u_1 & u_1 \otimes u_2 & u_1 \otimes u_3 \\ u_2 \otimes u_1 & u_2 \otimes u_2 & u_2 \otimes u_3 \\ u_3 \otimes u_1 & u_3 \otimes u_2 & u_3 \otimes u_3 \end{pmatrix} N_k = \begin{pmatrix} (F * G'_{1k}) \otimes (F * G'_{1k}) & (F * G'_{1k}) \otimes (F * G'_{2k}) & (F * G'_{1k}) \otimes (F * G'_{3k}) \\ (F * G'_{2k}) \otimes (F * G'_{1k}) & (F * G'_{2k}) \otimes (F * G'_{2k}) & (F * G'_{2k}) \otimes (F * G'_{3k}) \\ (F * G'_{3k}) \otimes (F * G'_{1k}) & (F * G'_{3k}) \otimes (F * G'_{2k}) & (F * G'_{3k}) \otimes (F * G'_{3k}) \end{pmatrix} \quad (6.66)$$

which can also be written as:

$$N_k^T \begin{pmatrix} u_1 \otimes u_1 & u_1 \otimes u_2 & u_1 \otimes u_3 \\ u_2 \otimes u_1 & u_2 \otimes u_2 & u_2 \otimes u_3 \\ u_3 \otimes u_1 & u_3 \otimes u_2 & u_3 \otimes u_3 \end{pmatrix} N_k = \begin{pmatrix} (F \otimes F) * (G'_{1k} \otimes G'_{1k}) & (F \otimes F) * (G'_{1k} \otimes G'_{2k}) & (F^S \otimes F^S) * (G'_{1k} \otimes G'_{3k}) \\ (F \otimes F) * (G'_{2k} \otimes G'_{1k}) & (F \otimes F) * (G'_{2k} \otimes G'_{2k}) & (F^S \otimes F^S) * (G'_{2k} \otimes G'_{3k}) \\ (F \otimes F) * (G'_{3k} \otimes G'_{1k}) & (F \otimes F) * (G'_{3k} \otimes G'_{2k}) & (F^S \otimes F^S) * (G'_{3k} \otimes G'_{3k}) \end{pmatrix} \quad (6.67)$$

Moment tensor

We have:

$$M_{pq} = \int \int_{\Sigma} m_{pq} d\Sigma = \int \int_{\Sigma} \mu(\nu_p[u_q] + \nu_q[u_p]) d\Sigma = \mu A(\nu_p[u_q] + \nu_q[u_p]) \quad (6.68)$$

where ν is the normal to the fault surface and $[u]$ is the displacement discontinuity on the fault.

We define a new coordinates system with the unit vectors $n^{(1)}$, $n^{(2)}$ and $n^{(3)}$, and the matrix N by:

$$N = \begin{pmatrix} n_1^{(1)} & n_1^{(2)} & n_1^{(3)} \\ n_2^{(1)} & n_2^{(2)} & n_2^{(3)} \\ n_3^{(1)} & n_3^{(2)} & n_3^{(3)} \end{pmatrix} \quad (6.69)$$

In the new coordinates system, the Green's function is equal to $G' = N^T G N$, the moment tensor to $M' = N^T M N$, and the displacement to $u' = N^T u$. We choose N such that:

$$M' = \mu D A \begin{pmatrix} 1 & 0 & 0 \\ 0 & -1 & 0 \\ 0 & 0 & 0 \end{pmatrix} \quad (6.70)$$

Therefore, we have:

$$u'_i \hat{\otimes} u'_j = (2\pi)^{\frac{3}{2}} \mu D^* A \left[\frac{\partial \hat{G}'_{i1}}{\partial \xi'_1} - \frac{\partial \hat{G}'_{i2}}{\partial \xi'_2} \right]^* \mu D A \left[\frac{\partial \hat{G}'_{j1}}{\partial \xi'_1} - \frac{\partial \hat{G}'_{j2}}{\partial \xi'_2} \right] \quad (6.71)$$

If we come back in the time domain, we have:

$$u'_i \otimes u'_j = \mu^2 A^2 (D * [\frac{\partial G'_{i1}}{\partial \xi'_1} - \frac{\partial G'_{i2}}{\partial \xi'_2}]) \otimes (D * [\frac{\partial G'_{j1}}{\partial \xi'_1} - \frac{\partial G'_{j2}}{\partial \xi'_2}]) \quad (6.72)$$

which can also be written as:

$$u'_i \otimes u'_j = \mu^2 A^2 (D \otimes D) * ([\frac{\partial G'_{i1}}{\partial \xi'_1} - \frac{\partial G'_{i2}}{\partial \xi'_2}] \otimes [\frac{\partial G'_{j1}}{\partial \xi'_1} - \frac{\partial G'_{j2}}{\partial \xi'_2}]) \quad (6.73)$$

If we choose N such that:

$$M' = \mu D A \begin{pmatrix} 1 & 0 & 0 \\ 0 & 0 & 0 \\ 0 & 0 & -1 \end{pmatrix} \quad (6.74)$$

we would get:

$$u'_i \otimes u'_j = \mu^2 A^2 (D \otimes D) * ([\frac{\partial G'_{i1}}{\partial \xi'_1} - \frac{\partial G'_{i3}}{\partial \xi'_3}] \otimes [\frac{\partial G'_{j1}}{\partial \xi'_1} - \frac{\partial G'_{j3}}{\partial \xi'_3}]) \quad (6.75)$$

If we choose N such that:

$$M' = \mu D A \begin{pmatrix} 0 & 0 & 0 \\ 0 & 1 & 0 \\ 0 & 0 & -1 \end{pmatrix} \quad (6.76)$$

we would get:

$$u'_i \otimes u'_j = \mu^2 A^2 (D \otimes D) * \left(\left[\frac{\partial G'_{i2}}{\partial \xi'_2} - \frac{\partial G'_{i3}}{\partial \xi'_3} \right] \otimes \left[\frac{\partial G'_{j2}}{\partial \xi'_2} - \frac{\partial G'_{j3}}{\partial \xi'_3} \right] \right) \quad (6.77)$$

How to compute the autocorrelation of the source term $F \otimes F$ or $D \otimes D$?

White noise At time t_i , we assume that the amplitude of the source function is A_i (random variable with expectancy $m = 0$ and standard deviation σ). We define a_i by:

$$P(A_i < p_0) = \int_{-\infty}^{p_0} a_i(p) dp \quad (6.78)$$

We have:

$$\int_{-\infty}^{\infty} a_i(p) dp = m \quad (6.79)$$

and:

$$\int_{-\infty}^{\infty} a_i^2(p) dp = m^2 + \sigma^2 \quad (6.80)$$

We suppose that the source function is a white noise, that is:

$$\int_{-\infty}^{\infty} (a_i(p) - m)(a_j(p) - m) dp = 0 \quad (6.81)$$

Thus, we have:

$$\int_{-\infty}^{\infty} a_i(p) a_j(p) dp = m^2 \quad (6.82)$$

We define the source time function $F(t_i) = A_i$ and we compute the autocorrelation. We have:

$$(F \otimes F)(t) = \int_{-\infty}^{\infty} F^*(\tau) F(t + \tau) d\tau \quad (6.83)$$

The expectancy of the term $F^*(\tau) F(t + \tau)$ is $m^2 + \sigma^2$ if $t = 0$ and m^2 if $t \neq 0$.

6.2.3 Stacking

6.3 Ray tracing

We solve the eikonal and the transport equations following Čeverský (2001, ch. 3.1).

6.3.1 Eikonal equation

Following Čeverský (2001, ch. 2.4), the eikonal equation is:

$$\nabla T \cdot \nabla T = \frac{1}{V^2} \quad (6.84)$$

with $V = \alpha$ or $V = \beta$. Using the Hamiltonian, it can also be written as:

$$\mathcal{H}(x_i, p_i) = \frac{1}{2} (p_i^2 - \frac{1}{V^2}) = 0 \quad (6.85)$$

where $p_i = \frac{\partial T}{\partial x_i}$.

We define the auxiliary variable σ by:

$$\frac{dx_i}{d\sigma} = \frac{\partial \mathcal{H}}{\partial p_i} \text{ and } \frac{dp_i}{d\sigma} = -\frac{\partial \mathcal{H}}{\partial x_i} \quad (6.86)$$

We get:

$$\frac{dT}{d\sigma} = \frac{\partial T}{\partial x_i} \frac{\partial x_i}{\partial \sigma} = p_i \frac{\partial \mathcal{H}}{\partial p_i} = \frac{1}{V^2} \quad (6.87)$$

thus we have:

$$T = T_0 + \frac{1}{V^2} \sigma \text{ and } \sigma = V^2(T - T_0) \quad (6.88)$$

Constant velocity

We have:

$$\frac{dp_i}{d\sigma} = -\frac{\partial \mathcal{H}}{\partial x_i} = \frac{1}{2} \frac{\partial}{\partial x_i} \left(\frac{1}{V^2} \right) = -\frac{1}{V^3} \frac{\partial V}{\partial x_i} = 0 \quad (6.89)$$

thus:

$$\begin{aligned} p_1 &= p_{10} \\ p_2 &= p_{20} \\ p_3 &= p_{30} \end{aligned} \quad (6.90)$$

We have:

$$x_i = x_{i0} + \frac{\partial \mathcal{H}}{\partial p_i} \sigma = x_{i0} + p_i \sigma \quad (6.91)$$

thus:

$$\begin{aligned} x_1 &= x_{10} + p_{10} V^2 (T - T_0) \\ x_2 &= x_{20} + p_{20} V^2 (T - T_0) \\ x_3 &= x_{30} + p_{30} V^2 (T - T_0) \end{aligned} \quad (6.92)$$

Constant gradient of velocity

We write the velocity as $V = az + b$.

We have:

$$\frac{dp_1}{d\sigma} = 0, \frac{dp_2}{d\sigma} = 0 \text{ and } \frac{dp_3}{d\sigma} = -\frac{1}{V^3} \frac{\partial V}{\partial z} = -\frac{a}{(az + b)^3} \quad (6.93)$$

thus:

$$\begin{aligned} p_1 &= p_{10} \\ p_2 &= p_{20} \\ p_3 &= p_{30} - \frac{a}{(az + b)^3} \sigma = p_{30} - \frac{a}{az + b} (T - T_0) \end{aligned} \quad (6.94)$$

We have:

$$\begin{aligned} x_1 &= x_{10} + p_{10} \sigma \\ x_2 &= x_{20} + p_{20} \sigma \\ x_3 &= x_{30} + p_{30} \sigma - \frac{1}{2} \frac{a}{(az + b)^3} \sigma^2 \end{aligned} \quad (6.95)$$

thus:

$$\begin{aligned} x_1 &= x_{10} + p_{10} (az + b)^2 (T - T_0) \\ x_2 &= x_{20} + p_{20} (az + b)^2 (T - T_0) \\ x_3 &= x_{30} + p_{30} (az + b)^2 (T - T_0) - \frac{1}{2} a (az + b) (T - T_0)^2 \end{aligned} \quad (6.96)$$

6.3.2 Transport equation

Following Čevertý (2001, ch. 2.4), the transport equation is:

$$2\nabla T \cdot \nabla (\sqrt{\rho V^2} A) + \sqrt{\rho V^2} A \nabla^2 T = 0 \quad (6.97)$$

with $V = \alpha$ or $V = \beta$ and A is the amplitude of the P-wave or one of the two components of the S-wave.

Constant velocity

We have $(\nabla T)_i = p_i = p_{i0}$ thus $\nabla^2 T = 0$ and the wave equation becomes:

$$2\nabla T \cdot \nabla (\sqrt{\rho V^2} A) = 0 \quad (6.98)$$

As ρ and V are constant, we get:

$$\nabla T \cdot \nabla A = p_i \frac{\partial A}{\partial x_i} = 0 \quad (6.99)$$

However, we have:

$$\frac{\partial A}{\partial \sigma} = \frac{\partial A}{\partial x_i} \frac{\partial x_i}{\partial \sigma} = \frac{\partial A}{\partial x_i} \frac{\partial \mathcal{H}}{\partial p_i} = \frac{\partial A}{\partial x_i} p_i \quad (6.100)$$

Thus:

$$\frac{\partial A}{\partial \sigma} = 0 \text{ that is } A = A_0 \quad (6.101)$$

Constant gradient of velocity

We have:

$$\nabla^2 T = \frac{a^2}{(az + b)^2} (T - T_0) \quad (6.102)$$

If we assume constant density, we get the transport equation:

$$2A \nabla T \cdot \nabla V + 2V \nabla T \cdot \nabla A + A \frac{a^2}{az + b} (T - T_0) = 0 \quad (6.103)$$

Chapter 7

Wavelet Analysis

The wavelet methods for time series analysis are explained in a more detailed way in Percival & Walden (2000 [35]).

7.1 Discrete Wavelet Transform

The Discrete Wavelet Transform (DWT) is an orthonormal transform that transforms a time series X_t ($t = 0, \dots, N - 1$) into a vector of wavelet coefficients W_i ($i = 0, \dots, N - 1$). If we denote J the level of the wavelet decomposition, and we have $N = n * 2^J$, where n is some integer higher or equal to 1, the vector of wavelet coefficients can be decomposed into J wavelet vectors W_j of lengths $\frac{N}{2}, \frac{N}{4}, \dots, \frac{N}{2^J}$, and one scaling vector V_J of length $\frac{N}{2^J}$.

Each wavelet vector W_j is associated with changes on scale $\tau_j = dt2^{j-1}$, where dt is the time step of the time series, and corresponds to the filtering of the original time series with a filter with nominal frequency interval $[\frac{1}{dt2^{j+1}}, \frac{1}{dt2^j}]$. The scaling vector V_J is associated with averages in scale $\lambda_J = dt2^J$, and corresponds to the filtering of the original time series with a filter with nominal frequency interval $[0, \frac{1}{dt2^{j+1}}]$.

We can also define for $j = 1, \dots, J$ the j th wavelet detail D_j , which is a vector of length N , and is associated to scale $\tau_j = dt2^{j-1}$. Similarly, we can define for $j = 1, \dots, J$ the j th wavelet smooth S_j , which is a vector of length N , and is associated to scales $\tau_{j+1} = dt2^{j+1}$ and higher. Together, the details and the smooths define the multiresolution analysis (MRA) of X :

$$X = \sum_{j=1}^J D_j + S_J \quad (7.1)$$

One main advantage of the DWT is that it is an orthonormal transform, and thus we can write the analysis of variance (ANOVA):

$$\|X\|^2 = \|W\|^2 = \sum_{j=1}^J \|W_j\|^2 + \|V_J\|^2 = \sum_{j=1}^J \|D_j\|^2 + \|S_J\|^2 \quad (7.2)$$

Moreover, the DWT can be computed using $O(N)$ multiplications.

However, the DWT present several disadvantages:

- The length of the time series must be a multiple of 2^J where J is the level of the DWT decomposition.
- The time step of the wavelet vector W_j is $dt2^j$, which may not correspond to the time when some interesting phenomenon is visible on the original time series.
- When we circularly shift the time series, the corresponding wavelet coefficients, details and smooths are not a circularly shifted version of the wavelet coefficients, details and smooths of the original time series. Thus, the values of the wavelet coefficients, details and smooths are strongly dependent on the time when we start experimentally gathering the data.
- When we filter the time series to obtain the details and smooths, we introduce a phase shift, which makes difficult to line up meaningfully the features of the MRA with the original time series.

7.2 Maximum Overlap Discrete Wavelet Transform

To get rid of these problems, we introduce the Maximum Overlap Discrete Wavelet Transform (MODWT). The MODWT transforms the time series X_t ($t = 0, \dots, N - 1$) into J wavelet vectors \tilde{W}_j ($j = 1, \dots, J$) of length N and a scaling vector \tilde{V}_J of length N . As is the case for the DWT, each wavelet vector \tilde{W}_j is associated with changes on scale $\tau_j = dt2^{j-1}$, and corresponds to the filtering of the original time series with a filter with nominal frequency interval $[\frac{1}{dt2^{j+1}}, \frac{1}{dt2^j}]$. The scaling vector \tilde{V}_J is associated with averages in scale $\lambda_J = dt2^J$, and corresponds to the filtering of the original time series with a filter with nominal frequency interval $[0, \frac{1}{dt2^{j+1}}]$.

As is the case for the DWT, we can write the MRA:

$$X = \sum_{j=1}^J \tilde{D}_j + \tilde{S}_J \quad (7.3)$$

and the ANOVA:

$$\|X\|^2 = \sum_{j=1}^J \|\tilde{W}_j\|^2 + \|\tilde{V}_J\|^2 \quad (7.4)$$

Now, we have the following properties:

- The MODWT of a time series can be defined for any length N .
- The time step of the wavelet vectors \tilde{W}_j and the scaling vector \tilde{V}_J is equal to the time step of the original time series.
- When we circularly shift the time series, the corresponding wavelet vectors, scaling vector, details and smooths are shifted by the same amount.
- The details and smooths are associated with a zero phase filter, making it easy to line up meaningfully the features of the MRA with the original time series.

However, the MODWT has some disadvantages over the DWT:

- The MODWT can only be computed using $O(N \log_2 N)$ multiplications.
- We can no longer write the ANOVA for the details and smooths:

$$\|X\|^2 \neq \sum_{j=1}^J \|D_j\|^2 + \|S_J\|^2 \text{ and } \|\tilde{W}_j\|^2 \neq \|\tilde{D}_j\|^2 \quad (7.5)$$

7.3 Discrete Wavelet Packet Transform

7.3.1 DWPT and MODWPT

When we carry out a DWT, we filter the time series X with the high-pass wavelet filter h_l ($l = 0, \dots, L - 1$) to obtain W_1 , and with the low-pass scaling filter g_l ($l = 0, \dots, L - 1$) to obtain V_1 . We then filter the vector of scaling coefficients at level 1 V_1 with the high-pass wavelet filter h_l ($l = 0, \dots, L - 1$) to obtain W_2 , and with the low-pass scaling filter g_l ($l = 0, \dots, L - 1$) to obtain V_2 . We thus get:

$$\mathcal{W}X = \begin{pmatrix} W_1 \\ W_2 \\ V_2 \end{pmatrix} = \begin{pmatrix} W_{1,1} \\ W_{2,1} \\ W_{2,0} \end{pmatrix} \quad (7.6)$$

We could have filtered the vector of wavelet coefficients at level 1 W_1 , instead of V_1 , and obtained:

$$\mathcal{W}X = \begin{pmatrix} W_{2,3} \\ W_{2,2} \\ W_{1,0} \end{pmatrix} \quad (7.7)$$

or we could have filtered both W_1 and V_1 , and obtained:

$$\mathcal{W}X = \begin{pmatrix} W_{2,3} \\ W_{2,2} \\ W_{2,1} \\ W_{2,0} \end{pmatrix} \quad (7.8)$$

At each level j , we can similarly carry out the Discrete Wavelet Packet Transform (DWPT) of X and obtain $n = 2^j$ wavelet vectors $W_{j,n}$ of length $\frac{N}{2^j}$, and corresponding to the filtering of the original time series with a filter with nominal frequency interval $[\frac{n}{dt2^{j+1}}, \frac{n+1}{dt2^{j+1}}]$.

The ANOVA decomposition becomes:

$$\|X\|^2 = \sum_{n=0}^{2^j-1} \|W_{j,n}\|^2 \text{ for each level } j \quad (7.9)$$

As we have done for the DWT, we can define for each level j the detail vectors $D_{j,n}$ ($n = 0, \dots, 2^j - 1$) of length N , and we get:

$$X = \sum_{n=0}^{2^j-1} D_{j,n} \text{ for each level } j \quad (7.10)$$

We can obtain the Maximum Overlap Discrete Wavelet Packet Transform (MODWPT) by filtering at each level j both \widetilde{W}_j and \widetilde{V}_j with the filters \widetilde{h}_l and \widetilde{g}_l . We thus get at each level j the wavelet vectors $\widetilde{W}_{j,n}$ ($n = 0, \dots, 2^j - 1$) of length N , and we have the properties:

$$\|X\|^2 = \sum_{n=0}^{2^j-1} \|\widetilde{W}_{j,n}\|^2 \text{ for each level } j \quad (7.11)$$

and:

$$X = \sum_{n=0}^{2^j-1} \widetilde{D}_{j,n} \text{ for each level } j \quad (7.12)$$

7.3.2 Best basis algorithm

At level $j = 2$, we can write the wavelet decomposition of X as one of the four decompositions:

$$\begin{pmatrix} W_{1,1} \\ W_{1,0} \end{pmatrix}, \begin{pmatrix} W_{2,1} \\ W_{2,0} \end{pmatrix}, \begin{pmatrix} W_{2,3} \\ W_{2,2} \\ W_{1,0} \end{pmatrix}, \text{ and } \begin{pmatrix} W_{2,3} \\ W_{2,2} \\ W_{2,1} \\ W_{2,0} \end{pmatrix} \quad (7.13)$$

To choose between these four decompositions, we define a cost functional:

$$M(W_{j,n}) = \sum_{t=0}^{N_j-1} m(|W_{j,n,t}|) \text{ with } N_j = \frac{N}{2^j} \quad (7.14)$$

and we try to minimize:

$$\min_{\mathcal{C}} \sum_{(j,n) \in \mathcal{C}} M(W_{j,n}) \quad (7.15)$$

with $\mathcal{C} \subset \mathcal{N}$ and $\mathcal{N} = \{(j, n) : j = 0, \dots, J; n = 0, \dots, 2^j - 1\}$. In the case of $J = 2$ above, we have 4 possible values for \mathcal{C} :

$$\begin{aligned} \mathcal{C}_1 &= \{(1, 0), (1, 1)\} \\ \mathcal{C}_2 &= \{(1, 1), (2, 0), (2, 1)\} \\ \mathcal{C}_3 &= \{(1, 0), (2, 2), (2, 3)\} \\ \mathcal{C}_4 &= \{(2, 0), (2, 1), (2, 2), (2, 3)\} \end{aligned}$$

7.3.3 Matching pursuit

Chapter 8

Long-range dependence

8.1 What is long-range dependence?

Time series: Any sequence of observations associated with an ordered independent variable t . For the analyses carried out in this report, we assume that the time series is defined essentially over a range of integers (usually $t = 0, 1, \dots, N - 1$, where N denotes the number of values in the time series).

Random variable: A real-valued random variable is a function, or mapping, from the sample space of possible outcomes of a random experiment to the real line.

Stochastic process: A discrete parameter real-valued stochastic process $\{X_t : t = \dots, -1, 0, 1, \dots\}$ is a sequence of random variables indexed over the integers. A process such as $\{X_t\}$ can serve as a stochastic model for a sequence of observations of some physical phenomenon. We assume that these observations are recorded at a sampling interval of Δt .

Stationarity: The process $\{X_t\}$ is said to be (second order) stationary if:

1. $E\{X_t\} = \mu_X$ for all integers t (i.e. μ_X does not depend on t).
2. $cov\{X_t, X_{t+\tau}\} = s_{X,\tau}$ for all integers t and τ (i.e. $s_{X,\tau}$ depends only on τ and does not depend on t).

Autocovariance sequence (ACVS): The sequence $\{s_{X,\tau} : \tau = \dots, -1, 0, 1, \dots\}$. The autocorrelation sequence (ACS) is $\rho_{X,\tau} = s_{X,\tau}/s_{X,0}$.

Spectral density function (SDF), or power spectrum: $S_X(f) = \Delta t \sum_{\tau=-\infty}^{\infty} s_{X,\tau} e^{-i2\pi f \tau \Delta t}$ for $|f| \leq f_N = \frac{1}{2\Delta t}$, that is $S_X(\cdot)$ is the Fourier transform of $\{s_{X,\tau}\}$.

Stationary long memory process: $\{X_t\}$ is a stationary long memory process if there exist constants α and C_S satisfying $-1 < \alpha < 0$ and $C_S > 0$ such that:

$$\lim_{f \rightarrow 0} \frac{S_X(f)}{C_S |f|^\alpha} = 1 \text{ that is } \log(S_X(f)) = \beta + \alpha \log(f) \quad (8.1)$$

8.2 Long-range dependence in low-frequency earthquake catalogs?

Episodic Tremor and Slip (ETS) is a phenomenon that takes place mostly in subduction zones, when a geodetically detected slow slip event occurs concurrently with tectonic tremor. Tremor is a long (several seconds to many minutes), low amplitude seismic signal, with emergent onsets, and an absence of clear impulsive phases. Their occurrence is correlated temporally and spatially with slow slip events on the subduction zone interface. At least a portion of the tremor is made of small low-frequency earthquakes (LFEs). LFEs group into families, or clusters of LFEs that repeat on small $\approx 1 \text{ km}^2$ patches on the plate interface.

For a given LFE family, we can obtain from the seismic data an event catalog that gives the exact timing (and sometimes the magnitude) of each small earthquake occurring on this given small patch. We can then construct a time series by counting the number of events occurring in every time windows of a given duration. For example, Frank *et al.* (2016) translated their LFE catalog from Guerrero, Mexico, into a discrete event count signal with regular time steps of 1 min, binning each catalogued event into the time step during which it is observed. They then computed an autocorrelation function for this time series. Finally, they computed the Fourier spectrum of the event count autocorrelation (see Figure 8.1).

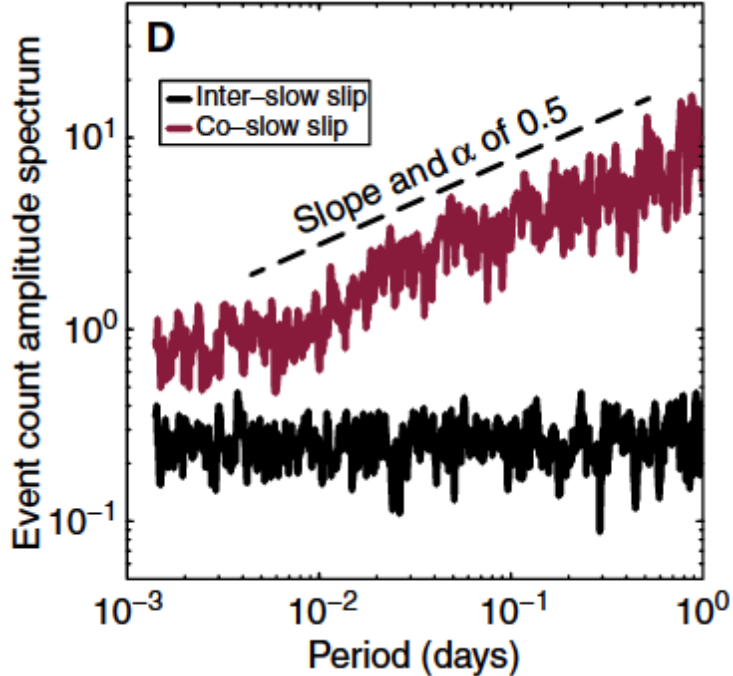


Figure 8.1: Figure 2D of Frank *et al.* (2016). We have $\log(S_X(f)) = \beta + \alpha \log(f)$ with $\alpha = -0.5$ where S_X is the spectral density function (SDF), or power spectrum, and f is the frequency.

I have taken a family of LFEs recorded in the Olympic Peninsula, Washington (catalog from Sweet *et al.*, 2014) and applied several estimators from Taqqu and Teverovsky (1998) to measure the intensity of long-range dependence in the event count time series.

Let us define a time series X_i , of length N . We define the corresponding aggregated series:

$$X^{(m)}(k) = \frac{1}{m} \sum_{i=(k-1)m+1}^{km} X_i, k = 1, 2, \dots, \left[\frac{N}{m} \right] \quad (8.2)$$

The first absolute moment of the time series is then:

$$AM^{(m)} = \frac{m}{N} \sum_{k=1}^{\frac{N}{m}} |X^{(m)}(k) - \bar{X}| \quad (8.3)$$

and $AM^{(m)}$ behaves as m^{H-1} , where H is the Hurst parameter. The result of the corresponding linear regression can be seen in Figure 8.2.

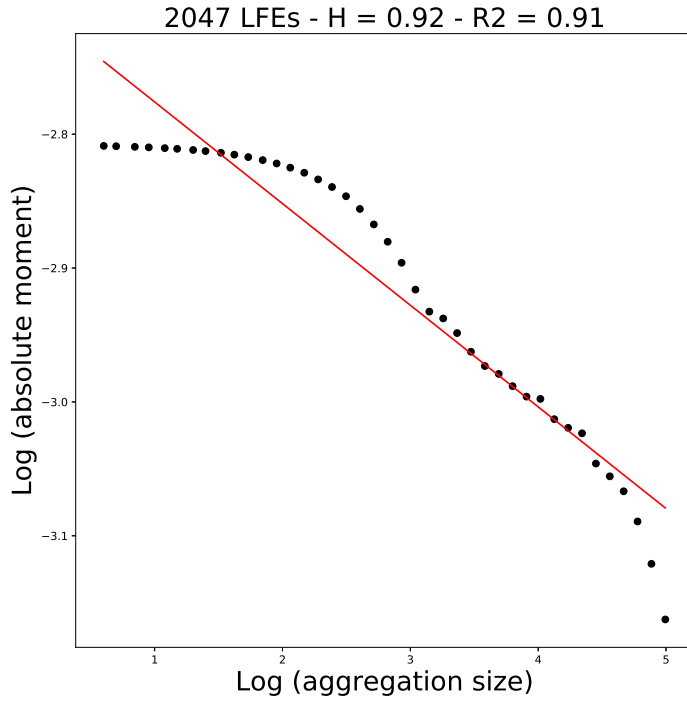


Figure 8.2: Estimation of the Hurst parameter with the absolute value method.

The sample variance of the time series is:

$$\hat{Var}X^{(m)} = \frac{m}{N} \sum_{k=1}^{\frac{N}{m}} \left(X^{(m)}(k) - \bar{X} \right)^2 \quad (8.4)$$

and $\hat{Var}X^{(m)}$ behaves as m^{2d-1} , where d is the fractional index. The result of the corresponding linear regression can be seen in Figure 8.3.

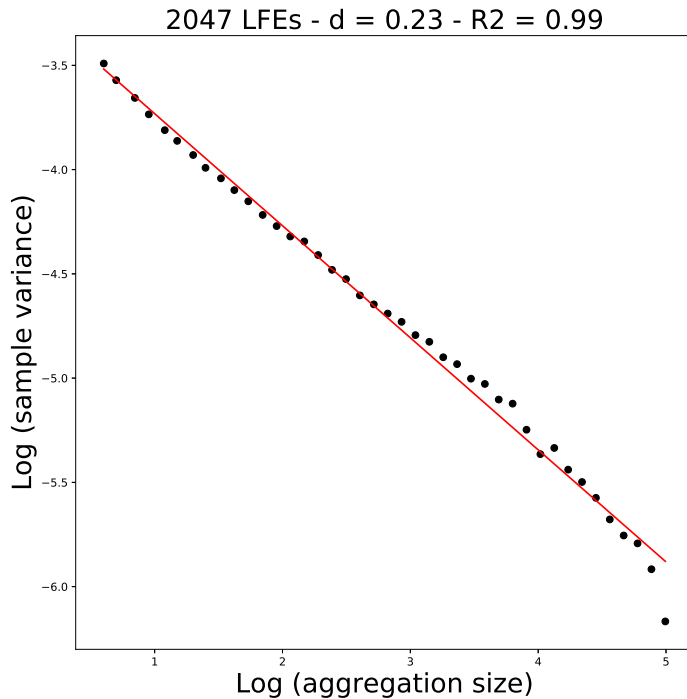


Figure 8.3: Estimation of the fractional index with the variance method.

To define the variance of residuals, we divide the time series into blocks of size m . We then compute the partial sums of the time series $Y(t) = \sum_{i=1}^t X_i$, and fit the partial sums within each block by a least-squares line $a + bt$. The sample variance $\frac{1}{m} \sum_{t=1}^m (Y(t) - a - bt)^2$ is then computed, and its average is proportional to m^{2d+1} . The result of the corresponding linear regression can be seen in Figure 8.4.

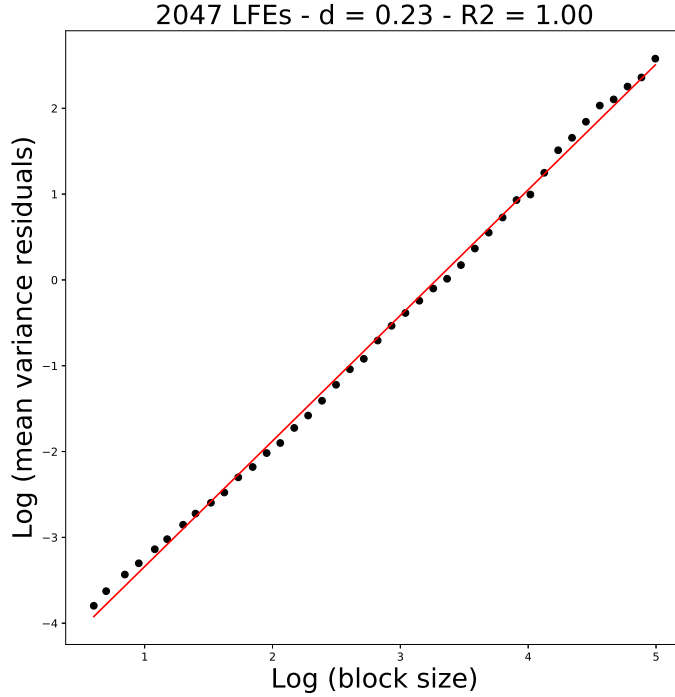


Figure 8.4: Estimation of the fractional index with the variance of residuals method.

The R/S statistics is defined by:

$$R(t, k) = \max_{0 \leq i \leq k} \left[Y_{t+i} - Y_t - \frac{i}{k} (Y_{t+k} - Y_t) \right] - \min_{0 \leq i \leq k} \left[Y_{t+i} - Y_t - \frac{i}{k} (Y_{t+k} - Y_t) \right] \quad (8.5)$$

$$S(t, k) = \sqrt{\frac{1}{k} \sum_{i=t+1}^{t+k} (X_i - \bar{X}_{t,k})^2} \quad (8.6)$$

and $R/S = \frac{R(t,k)}{S(t,k)}$ behaves as $k^{d+1/2}$. The result of the corresponding linear regression can be seen in Figure 8.5.

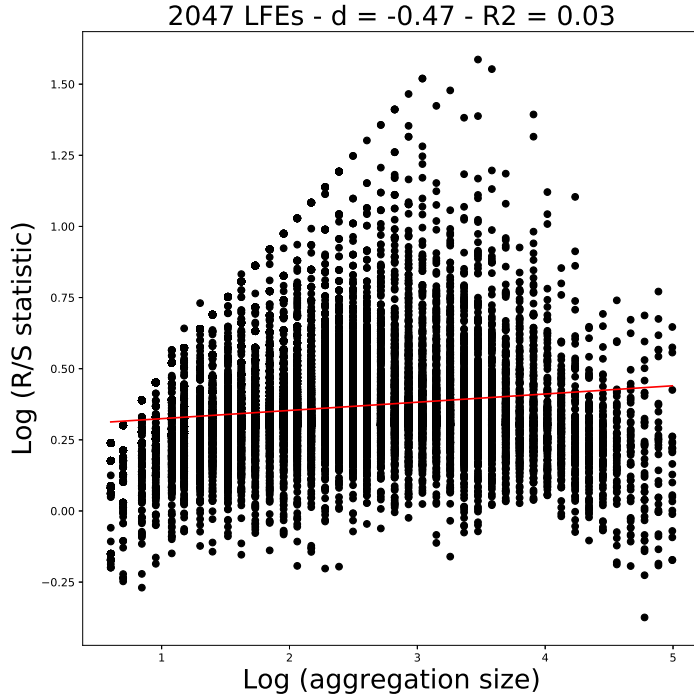


Figure 8.5: Estimation of the fractional index with the R/S method.

The periodogram is defined as:

$$I(\nu) = \frac{1}{2\pi N} \left| \sum_{j=1}^N X(j) e^{ij\nu} \right|^2 \quad (8.7)$$

and $I(\nu)$ behaves as $|\nu|^{-2d}$ close to the origin. The result of the corresponding linear regression can be seen in Figure 8.6.

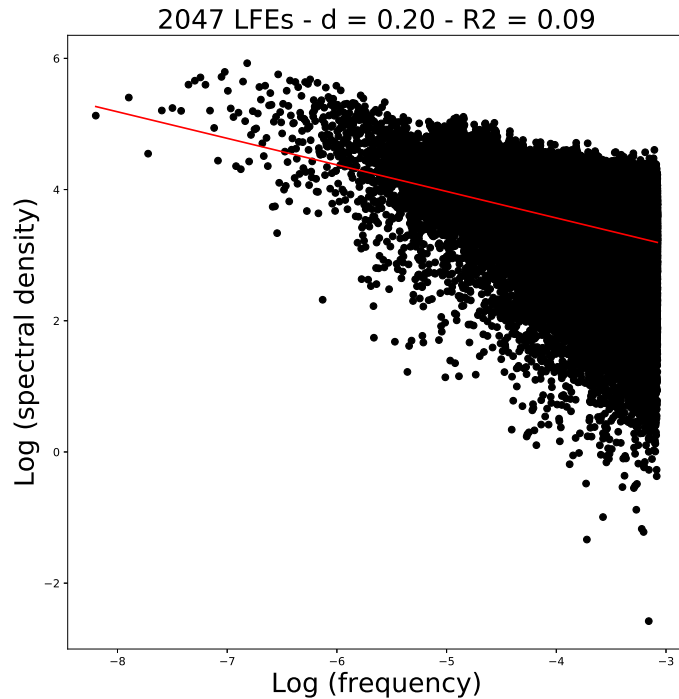


Figure 8.6: Estimation of the fractional index with the periodogram method.

Frank, WB ; Shapiro, NM ; Husker, AL ; Kostoglodov, V ; Gusev, AA ; Campillo, M. The evolving interaction of low-frequency earthquakes during transient slip. *Science Advances*, 2016 Apr, Vol.2(4).

Sweet, Justin R. ; Creager, Kenneth C. ; Houston, Heidi. A family of repeating lowfrequency earthquakes at the downdip edge of tremor and slip. *Geochemistry, Geophysics, Geosystems*, September 2014, Vol.15(9), pp.3713-3721.

Murad S. Taqqu and Vadim Teverovsky. On estimating the intensity of long-range dependence in finite and infinite variance time series. In: *A practical guide to heavy tails : statistical techniques and applications*. Robert J. Adler; Raisa E. Feldman, 1958-; Murad S. Taqqu; 1998 Boston : Birkhäuser.

Part IV

Time lags

Chapter 9

Data

9.1 Description of the dataset

The available data come from eight small-aperture arrays installed in the eastern part of the Olympic Peninsula. The aperture of the arrays is about 1 km, and station spacing is a few hundred meters. The arrays are around 5 to 10 km apart from each other. Most of the arrays were installed for nearly a year and were able to record the main August 2010 ETS event, and some of the stations were able to record the August 2011 ETS event. The time and locations of the tremor sources were all computed by Ghosh *et al.* (2012 [15]).

9.2 Websites to access the data

9.2.1 FDSN

International Federation of Digital Seismograph Networks

This website gives a list of the network codes, and the corresponding map, with the names and locations of stations. The selected experiments are:

- XG (2009-2011): Cascadia Array of Arrays
- XU (2006-2012): Collaborative Research: Earthscope integrated investigations of Cascadia subduction zone tremor, structure and process

The stations are the following:

- Port Angeles XG - PA01 to PA13
- Danz Ranch XG - DR01 to DR10, and DR12
- Lost Cause XG - LC01 to LC14
- Three Bumps XG - TB01 to TB14
- Burnt Hill XG - BH01 to BH11
- Cat Lake XG - CL01 to CL20
- Gold Creek XG - GC01 to GC14
- Blyn XU - BS01 to BS06, BS11, BS20 to BS27

9.2.2 IRIS

IRIS DMC MetaData Aggregator

This website gives for each station:

- Location and time of recording
- Epoch (effective periods of recording during the time that the station was installed)

- Type of instrument
- Channels

The data can be downloaded from the IRIS DMC using the Python package `obspy`, and the subpackage `obspy.clients.fdsn`, or alternatively, they can be downloaded from the ESS server Rainier, using the subpackage `obspy.clients.earthworm`.

9.2.3 PNSN

Pacific Northwest Seismic Network tremor catalog

This website gives the dates and locations of tremor activity in Cascadia. Following Ghosh *et al.* (2012 [15]), the selected periods of tremors are:

- From November 9th 2009 to November 13th 2009,
- From March 16th 2010 to March 21st 2010,
- From August 14th 2010 to August 22nd 2010.

Chapter 10

Method

10.1 Is the method going to work?

We assume that each tremor source is located on the plate boundary and generates a direct P-wave and a direct S-wave, and P-to-P, S-to-S, P-to-S, and S-to-P reflections off both the slab Moho and a mid-slab crustal discontinuity caused by the inferred strong velocity contrast between the hydrated basaltic upper oceanic crust, and the impermeable gabbroic lower oceanic crust. There is a time lag between the arrival of the direct wave and the arrivals of the reflected waves at a seismic station. By computing the autocorrelation or the cross correlation of the seismic signal recorded at the station, we expect to see an amplitude peak at each time lag corresponding to the time difference between two different phase arrivals.

The first question is which are the phases that we can expect to see on the auto / cross correlation signal, that is which phases have a high enough amplitude to be seen on the auto / cross correlation signal. We assumed a simple velocity model with four parallel dipping layers (continental crust, upper oceanic crust, lower oceanic crust, and oceanic mantle). Using Snell's law and the reflection / transmission coefficients from Aki and Richards (2002 [1]), we computed for different positions of the tremor source, the amplitude of the direct P- and S-waves, and the amplitude of the reflected and converted waves, and we looked at the amplitude ratio between both phases (see Jupyter notebook AmplitudesOnGrid.ipynb). On the horizontal autocorrelation plot, we can expect to see:

- A peak corresponding to the time lag between the direct S-wave and the reflected SH-wave on the mid-slab discontinuity,
- A peak corresponding to the time lag between the direct S-wave and the reflected SH-wave on the Moho, and
- A peak corresponding to the time lag between the direct S-wave and a ray corresponding to a P-wave traveling downward, converted to an S-wave at the Moho, and traveling upward.

On the vertical autocorrelation plot, we can expect to see:

- A peak corresponding to the time lag between the direct P-wave and the reflected P-wave at the mid-slab discontinuity.

On the cross correlation plot, we can expect to see:

- A peak corresponding to the time lag between the direct P-wave and the direct S-wave,
- A peak corresponding to the time lag between the direct P-wave and the reflected SH-wave on the mid-slab discontinuity,
- A peak corresponding to the time lag between the direct P-wave and the reflected SH-wave on the Moho, and
- A peak corresponding to the time lag between the direct P-wave and a ray corresponding to a P-wave traveling downward, converted to an S-wave at the Moho, and traveling upward.

The second question is at which time lag should we expect to see this peaks. We computed the time arrival for all of the waves above (see Jupyter notebook TimeDifferenceArray.ipynb). On the autocorrelation plots, all the peaks should be seen between 0 and 5 seconds. On the cross correlation plots, all the peaks should be seen between 1 and 14 seconds. We do not expect peaks on the negative part of the cross correlation plots.

We are going to stack the seismograms recorded at different stations of the same array. The third questions is thus whether we need to apply some time shift to the seismic recordings before stacking them. For that, we need to know whether there is a significant difference between the time lags at different stations from the same array. To answer this question, we computed for each station the time lag between the direct P/S wave arrival, and the arrival of the PPP and SH waves reflected off the mid-slab discontinuity, and the PPSSS and SH waves reflected off the Moho (see Jupyter notebook TimeLagOnGrid.ipynb).

Then, we computed the average difference in time lag between two stations. We found that the difference in time lags between two stations of the same array stays always inferior to 0.1 second. We can thus stack the seismograms over all the stations, without applying some time shift between the stations.

The location of the tremor source is not constant with time. During an ETS event, rapid tremor streaks have been observed propagating in the up-dip and down-dip directions at velocities ranging on average between 30 and 110, and up to 200 km/h, which corresponds to a source displacement of 0.5 to 3 km during one minute. If we denote t_d the arrival time of the direct wave, and t_r the arrival time of the reflected wave, the time lag between the two phase arrivals is $t_{lag} = t_d - t_r$. During the one-minute time window where we compute the auto / cross correlation, the displacement dx of the tremor source along the plate boundary should corresponds to a time lag difference dt_{lag} shorter than a quarter of the dominant period of $T = 0.3$ s. We computed the time lag difference for a displacement of the source of 0.5, 1.8 and 3 km in the up-dip direction, for stations aligned along the strike and along the dip direction. We assume that the source was located at 35 kilometres depth, and we look at the time arrivals of the seismic wave for stations located up to 20 kilometres from the epicentre, in the strike or the dip direction (see Jupyter notebook TimeDifferenceStrikeDip.ipynb). The difference in time lags stays low for all the stations aligned along the strike of the plate boundary, even for tremor streaks travelling at 200 km/h. However, for the stations aligned along the dip of the plate boundary, the tremor streaks travelling at 200 km/h will cause a problem for the stations that are not immediately above the tremor source. The tremor streaks travelling at 110 km/h will cause a problem for the stations located more than 6 km updip of the tremor source.

Chapter 11

Results

11.1 Tremor just under the array

We first look at the cross correlation of the horizontal components and the vertical component of the seismograms recorded at the Big Skidder array when the tremor source is located in a five by five kilometres square cell centered on this array. Using Snell's law and assuming a simple velocity model with four parallel dipping layers (continental crust, upper oceanic crust, lower oceanic crust, and oceanic mantle), we compute the time arrival of the direct P-wave, the direct S-wave, and the downgoing P-wave reflected at the mid-slab discontinuity, and then travelling upward. We assume that the tremor source is located at the plate boundary, and we take the depth of the plate boundary from McCrory *et al.* (2006 [26]), that is the depth is 41.5 km.

For the values of the seismic velocities, we made a first hypothesis: The P-wave velocity of the continental crust is taken from Bostock *et al.* (2015 [8], 1D model from their Table 1, 6 to 30 km depth). We assumed a V_P/V_S ratio of $\sqrt{3}$, and we computed the density from Gardner's law ($\rho = 1000 * 0.31 * V_P^{0.25}$). The P-wave velocity, S-wave velocity, density, and thickness of the upper oceanic crust are taken from Nowack and Bostock (2013 [31], velocity model for their template 37). The P-wave velocity, S-wave velocity, and density of the lower oceanic crust are from Nowack and Bostock (2013 [31]). We assume a total thickness of the oceanic crust of 7 kilometres. The P-wave velocity, S-wave velocity, and density of the oceanic mantle is from Nikulin *et al.* (2009 [30], last layer of 1D model under station GNW, located in the eastern Olympic Peninsula, from their Table 2). All values are given in Table 11.1. With these values, we get the time arrival of the direct P-wave (5.84 s), the time arrival of the direct S-wave (10.12 s), and the time arrival of the reflected P-wave at the mid-slab discontinuity (7.25 s), which gives us a time lag between the direct P- and S-waves of 4.28 s, and a time lag between the direct S-wave and the reflected P-wave of 2.87 s.

Layer	V_P (m/s)	V_S (m/s)	ρ (kg/m ³)	Thickness (m)
Continental crust	7100	4099	2846	-
Upper oceanic crust	4600	1949	2700	3300
Lower oceanic crust	7000	3400	3000	3700
Oceanic mantle	8000	4600	2932	-

Table 11.1: Seismic velocities, densities and thicknesses of first layered model.

We then made a second hypothesis. The P-wave velocity, and the S-wave velocity of the continental crust is taken from Nikulin *et al.* (2009 [30], first layer of 1D model under station GNW, from their Table 2), and we computed the density from Gardner's law ($\rho = 1000 * 0.31 * V_P^{0.25}$). The P-wave velocity, S-wave velocity, density, and thickness of the upper oceanic crust are taken from Nowack and Bostock (2013 [31], velocity model for their template 14). The values for the lower oceanic crust and the oceanic mantle stay unchanged. All values are given in Table 11.2. With these values, we get the time arrival of the direct P-wave (6.69 s), the time arrival of the direct S-wave (12.03 s), and the time arrival of the reflected P-wave at the mid-slab discontinuity (8.03 s), which gives us a time lag between the direct P- and S-waves of 5.33 s, and a time lag between the direct S-wave and the reflected P-wave of 3.99 s.

Layer	V_P (m/s)	V_S (m/s)	ρ (kg/m ³)	Thickness (m)
Continental crust	6200	3450	2751	-
Upper oceanic crust	4800	2133	2700	3300
Lower oceanic crust	7000	3400	3000	3700
Oceanic mantle	8000	4600	2932	-

Table 11.2: Seismic velocities, densities and thicknesses of second layered model.

In both cases, the amplitude ratio between the direct S-wave and the direct P-wave is about 2.5 times the amplitude ratio between the direct S-wave and the reflected P-wave at the mid-slab discontinuity. In the cross correlation plot with linear stacking, we can see a main peak at 4.7 s, and a secondary peak at 3.0 s, which amplitude is about half the amplitude of the main cross correlation peak. We hypothesize that the main peak represents the time lag between the direct P-wave and the direct S-wave, and that the secondary peak represents the time lag between the direct S-wave and the reflected P-wave at the mid-slab discontinuity.

However, if we assume that there is no mid-slab discontinuity, and that the entire oceanic crust has the rheological properties of the lower oceanic crust defined above, the lag time between the direct S-wave and a reflected P-wave on the Moho would be equal to 2.33 s (with the first set of parameters from Bostock *et al.* (2015 [8] for the continental crust) or to 3.39 s (with the second set of parameters from Nikulin *et al.* (2009 [30] for the continental crust. However, the amplitude ratio between the direct S-wave and the reflected P-wave at the Moho would be about three to four times smaller than in the case of a reflection at the mid-slab discontinuity. The first scenario with a reflection on a mid-slab discontinuity is therefore more likely.

In both cases, we expect to see a peak on the autocorrelation of the vertical component, corresponding to the time lag between the direct P-wave and the reflected P-wave on the mid-slab discontinuity or the Moho. However, this peak should be located at about 1.34 to 1.40 s (for the reflection on the mid-slab discontinuity), or 1.94 to 1.95 s (for the reflection on the Moho), and would be hard to see on the autocorrelation signal.

Finally, if we assume that there is a Low Velocity Zone (LVZ) and that it corresponds to the entire oceanic crust, and has the same rheological properties of the upper oceanic crust defined above, we could expect to see on the horizontal-to-vertical cross correlation signal, a peak at 1.30 to 2.48 s corresponding to the time lag between the direct S-wave and the reflected P-wave at the Moho, and a peak at 4.28 to 5.33 s corresponding to the time lag between the direct P-wave and the direct S-wave. However, due to the strong velocity contrast between the seismic wave velocities in the LVZ and in the oceanic mantle, we also expect on the vertical autocorrelation a peak at 2.85 to 2.98 s corresponding to the time lag between the direct P-wave and the reflected P-wave on the Moho ; and on the horizontal-to-vertical cross correlation a peak at 11.33 to 11.77 s corresponding to the time lag between the direct P-wave and the reflected S-wave on the Moho. We do not see any of these peaks and conclude that this last scenario is unlikely.

11.2 Different locations of the tremor

Latitude	Longitude	Depth	Model 1	Model 2	Model 3	Model 4	Data
47.9124	-122.9957	40.1464	4.20	5.24	4.20	5.24	4.8
47.9573	-122.9957	40.3390	4.19	5.23	4.19	5.23	4.85
48.0022	-122.9957	40.5549	4.24	5.29	4.24	5.29	4.7
47.9124	-122.9287	41.2982	4.29	5.35	4.29	5.35	4.85
47.9573	-122.9287	41.4877	4.28	5.33	4.28	5.33	4.85
48.0022	-122.9287	41.7000	4.33	5.40	4.33	5.40	4.95
47.9124	-122.8616	42.4448	4.44	5.53	4.44	5.53	5.0
47.9573	-122.8616	42.6332	4.43	5.52	4.43	5.52	6.3
48.0022	-122.8616	42.8438	4.48	5.58	4.48	5.58	5.5

Table 11.3: Expected position of the main cross correlation peak (direct S-wave and direct P-wave).

Latitude	Longitude	Depth	Model 1	Model 2	Model 3	Model 4	Data
47.9124	-122.9957	40.1464	2.79	3.89	2.23	3.27	
47.9573	-122.9957	40.3390	2.77	3.86	2.21	3.24	
48.0022	-122.9957	40.5549	2.82	3.93	2.26	3.32	
47.9124	-122.9287	41.2982	2.86	3.98	2.30	3.36	
47.9573	-122.9287	41.4877	2.84	3.96	2.28	3.34	
48.0022	-122.9287	41.7000	2.92	4.05	2.38	3.46	
47.9124	-122.8616	42.4448	3.01	4.17	2.46	3.56	
47.9573	-122.8616	42.6332	3.02	4.18	2.49	3.59	
48.0022	-122.8616	42.8438	3.09	4.27	2.59	3.72	

Table 11.4: Expected position of the secondary cross correlation peak (direct S-wave and reflected P-wave on the mid-slab or the Moho).

Latitude	Longitude	Depth	Model 1	Model 2	Model 3	Model 4	Data
47.9124	-122.9957	40.1464	1.41	1.35	1.97	1.97	
47.9573	-122.9957	40.3390	1.42	1.36	1.98	1.98	
48.0022	-122.9957	40.5549	1.43	1.37	1.98	1.98	
47.9124	-122.9287	41.2982	1.43	1.37	1.99	1.99	
47.9573	-122.9287	41.4877	1.43	1.37	2.00	2.00	
48.0022	-122.9287	41.7000	1.41	1.35	1.95	1.94	
47.9124	-122.8616	42.4448	1.43	1.36	1.98	1.97	
47.9573	-122.8616	42.6332	1.40	1.34	1.94	1.92	
48.0022	-122.8616	42.8438	1.38	1.31	1.89	1.86	

Table 11.5: Expected position of the vertical autocorrelation peak (direct P-wave and reflected P-wave on the mid-slab or the Moho).

Chapter 12

Discussion and things to do

- Write work already done
- Read paper by Korenaga
- Implementation tf-PHS stacking
- Implementation noise computation (from Korenaga paper)
- Scripts to download and store tremor data
- Script to compute MODW(P)T and scattering transform (and then CC)

Part V

LFE catalog

Chapter 13

Data

13.1 Description of the dataset

The template waveforms are the ones obtained by Plourde *et al.* (2015, [36]). Alexandre Plourde has kindly provided us his template files.

The folder *waveforms* contains 91 Matlab files, which contain the template waveforms for the three channels of each of the stations. The folder *detections* contains 89 files, which contain the names of the stations that were used by the network matched filter, and the time of each LFE detection. 66 of these templates have then been grouped into 34 families. The names of the templates in each family are given in the file *family_list.m*. The locations of the hypocentre for each template are given in the file *template_locations.txt*. The locations of the hypocentre for each family are given in the file *unique_families_NCAL.txt*.

13.2 Websites to access the data

The waveforms from the FAME experiment can be accessed from the IRIS DMC using the Python package obspy, and the subpackage obspy.clients.fdsn. The network code is XQ, and the stations names are ME01 to ME93.

The waveforms for the permanent stations of the Northern California Seismic Network can be downloaded from the website of the Northern California Earthquake Data Center (NCEDC). The stations are B039 from the network PB, KCPB, KHBB, KRMB, and KSXB from the network NC, and WDC and YBH from the network BK. Queries for downloading the data in the miniSEED format must be formated as explained here:

FDSN Dataselect

The instrument response can be obtained from here:

FDSN Station

Chapter 14

Method

Chapter 15

Results

Chapter 16

Discussion and things to do

Look at the maximum of the envelope (instead of the maximum of the raw signal) to find the time of the LFE.

Part VI

Slow slip

Chapter 17

Introduction

- Some generalities about slow slip and tremor
- A few words about what wavelets are
- Short bibliography about what has been done (master Sequoia Alba + papers by Ohtani and Wei)

The goal of this research work is to study the change over time in the spectral content of recordings of surface displacement by GPS stations, in order to detect slow slip events.

What I hope to do with that:

- Maybe by combining wavelet analyses of several channels and several stations, we will be able to detect smaller inter-ETS events, which can currently be observed in the tremor catalogs, but not in the GPS data.
- Maybe by looking at the wavelet details at larger scale, we could see some long term events (but we need to find a way to deal with the missing data before that).
- We could use wavelets to do some denoising of the vertical component of the GPS data. That could be useful to invert the slip at the surface and get the maximum depth of the slip on the plate boundary.
- Which region would be more interesting to study? All Cascadia? Only some areas not very well covered?

17.1 New Zealand

Slow slip in 2004 but no tremor. Instead, increase in microseismicity (Delahaye et al., 2009). Possible explanation is shallower depth (15-20 km) of the slow slip.

Shallow (15-20 km) and deep (25-60 km) slow slip events. Tremor downdip of the slow slip (Bartlow et al., 2014) but microseismicity.

Challenging tremor detection. Most abundant during large magnitude SSE. Deep inland tremor with possible undetected long-term SSE. (Todd and Schwartz, 2016)

Chapter 18

Data

We use the GPS data collected and made available on the website of the Pacific Northwest Geodetic Array (PANGA), from Central Washington University. Three types of time series are available:

- Raw data recorded by the GPS stations, after GIPSY postprocessing.
- Detrended data, for which a linear trend corresponding to the secular plate motion has been removed from the data.
- Cleaned data, for which the linear trend, steps due to earthquakes or hardware upgrades, and annual and semi-annual sinusoids signals have been simultaneously estimated and removed following Szeliga *et al.* (2008 [46]). Surface loading due to hydrology and atmospheric pressure introduces an annual signal in the GPS time series with respect to a global reference frame. This annually repeating component also introduces power at all harmonic frequencies, thus it may also be necessary to remove a semi-annual sinusoid from the raw data (Blewitt and Lavallée, 2002 [5]).

For each GPS station, the website provides a file for the three components of the displacement (latitude, longitude, and vertical), and each file contains three columns, corresponding to the time, the displacement (in millimetres), and the error. The data are recorded once a day.

The raw data are filtered with the function $f(t)$ to obtain the detrended, and then the cleaned data:

$$f(t) = \text{line}(t) + (\text{annual} + \text{semi-annual})(t) + \text{jumps}(t) \quad (18.1)$$

with:

$$\text{line}(t) = p_1 + p_2 t \quad (18.2)$$

$$(\text{annual} + \text{semi-annual})(t) = p_3 \sin(2\pi t + p_4) + p_5 \sin(4\pi t + p_6) \quad (18.3)$$

$$\text{jumps}(t) = \sum_{i=1}^n p_i \text{Heaviside}(t - t_i) \quad (18.4)$$

The values of the p_i and t_i are given at the beginning of each file. The best linear unbiased estimates of the model parameters p_i are computed using an orthogonal-triangular decomposition, or QR-factorization (Nikolaidis, 2002 [29]).

Chapter 19

Method

The Discrete Wavelet Transform (DWT) is an orthonormal transform that uses a sequence of filtering operations to associate a time series $X_t (t = 0, \dots, N - 1)$ written in the traditional orthonormal basis:

$$\mathbf{X} = X_0 \begin{pmatrix} 1 \\ 0 \\ 0 \\ \cdot \\ \cdot \\ 0 \end{pmatrix} + X_1 \begin{pmatrix} 0 \\ 1 \\ 0 \\ \cdot \\ \cdot \\ 0 \end{pmatrix} + X_2 \begin{pmatrix} 0 \\ 0 \\ 1 \\ \cdot \\ \cdot \\ 0 \end{pmatrix} + \dots + X_{N-1} \begin{pmatrix} 0 \\ 0 \\ 0 \\ \cdot \\ \cdot \\ 1 \end{pmatrix} \quad (19.1)$$

with the wavelet coefficients $W_t (t = 0, \dots, N - 1)$, which is the same time series written in another orthonormal basis:

$$\mathbf{X} = W_0 \begin{pmatrix} \mathcal{W}_{0,0} \\ \mathcal{W}_{0,1} \\ \mathcal{W}_{0,2} \\ \cdot \\ \cdot \\ \mathcal{W}_{0,N-1} \end{pmatrix} + W_1 \begin{pmatrix} \mathcal{W}_{1,0} \\ \mathcal{W}_{1,1} \\ \mathcal{W}_{1,2} \\ \cdot \\ \cdot \\ \mathcal{W}_{1,N-1} \end{pmatrix} + W_2 \begin{pmatrix} \mathcal{W}_{2,0} \\ \mathcal{W}_{2,1} \\ \mathcal{W}_{2,2} \\ \cdot \\ \cdot \\ \mathcal{W}_{2,N-1} \end{pmatrix} + \dots + W_{N-1} \begin{pmatrix} \mathcal{W}_{N-1,0} \\ \mathcal{W}_{N-1,1} \\ \mathcal{W}_{N-1,2} \\ \cdot \\ \cdot \\ \mathcal{W}_{N-1,N-1} \end{pmatrix} \quad (19.2)$$

where the $\mathcal{W}_{t,.}$ ($t = 0, \dots, N - 1$) are the wavelet basis vectors. The main advantage of the wavelet transform is that it captures information about both the frequency and the temporal content of the input data. This is contrasted with the Fourier transform, which characterizes the amplitude and phase of the frequency content only. Indeed, a local perturbation of the initial time series will affect all the coefficients of the Fourier transform, whereas it will only affect a few wavelet coefficients around the time of the perturbation.

The first $\frac{N}{2}$ $\mathcal{W}_{t,.}$ ($t = 0, \dots, \frac{N}{2} - 1$) wavelet basis vectors are circularly shifted with each other:

$$\mathcal{W}_{k,j} = \mathcal{W}_{i,j+2(i-k)} \quad (19.3)$$

and their Fourier transform has a nominal frequency band of $[\frac{1}{4dt}; \frac{1}{2dt}]$, where dt is the time step of the time series. We can write their coordinates as:

$$\mathcal{W}_{t,l} = h_l^o \quad t = 0, \dots, \frac{N}{2} - 1, l = 0, \dots, N - 1 \quad (19.4)$$

where h_l^o ($l = 0, \dots, N - 1$) is the wavelet filter.

The first wavelet vector \mathbf{W}_1 has length $\frac{N}{2}$, and is associated with changes on scale $\tau_1 = dt$. We can get its coefficients $W_{1,t}$ ($t = 0, \dots, \frac{N}{2} - 1$) by computing the scalar product of the first $\frac{N}{2}$ $\mathcal{W}_{t,.}$ ($t = 0, \dots, \frac{N}{2} - 1$) wavelet basis vectors with the time series \mathbf{X} :

$$W_{1,t} = \sum_{j=0}^{N-1} \mathcal{W}_{t,j} X_j, \quad t = 0, \dots, \frac{N}{2} - 1 \quad (19.5)$$

The new time series \mathbf{W}_1 has time step $2dt$, and corresponds to the filtering of the original time series with a filter with nominal frequency interval $[\frac{1}{4dt}; \frac{1}{2dt}]$.

The next $\frac{N}{4}$ $\mathcal{W}_{t,i}$, ($t = \frac{N}{2}, \dots, \frac{3N}{4} - 1$) wavelet basis vectors are also circularly shifted with each other:

$$\mathcal{W}_{k,j} = \mathcal{W}_{i,j+4(i-k)} \quad (19.6)$$

and their Fourier transform has a nominal frequency band of $[\frac{1}{8dt}; \frac{1}{4dt}]$. We can write their coordinates as:

$$\mathcal{W}_{\frac{N}{2}+t,l} = \sum_{j=0}^{N-1} g_{j-l \mod N}^o h_{4t+3-j \mod N}^{o\uparrow}, t = 0, \dots, \frac{N}{4} - 1, l = 0, \dots, N - 1 \quad (19.7)$$

where $\mathbf{h}^{o\uparrow}$ is formed by inserting a 0 between each of the elements of \mathbf{h}^o , and g_l^o ($l = 0, \dots, N - 1$) is the scaling filter defined by:

$$g_l^o = (-1)^{l+1} h_{N-1-l}^o, l = 0, \dots, N - 1 \quad (19.8)$$

The second wavelet vector \mathbf{W}_2 has length $\frac{N}{4}$, and is associated with changes on scale $\tau_2 = 2dt$. We can get its coefficients $W_{2,t}$ ($t = 0, \dots, \frac{N}{4} - 1$) by computing the scalar product of the next $\frac{N}{4}$ $\mathcal{W}_{t,i}$, ($t = \frac{N}{2}, \dots, \frac{3N}{4} - 1$) wavelet basis vectors with the time series \mathbf{X} :

$$W_{2,t} = \sum_{j=0}^{N-1} \mathcal{W}_{\frac{N}{2}+t,j} X_j, t = 0, \dots, \frac{N}{4} - 1 \quad (19.9)$$

The new time series \mathbf{W}_2 has time step $4dt$, and corresponds to the filtering of the original time series with a filter with nominal frequency interval $[\frac{1}{8dt}; \frac{1}{4dt}]$.

At the level J , we can write the orthonormal transform as:

$$\mathbf{W} = \mathcal{W}\mathbf{X} \text{ or } \begin{pmatrix} \mathbf{W}_1 \\ \mathbf{W}_2 \\ \mathbf{W}_3 \\ \vdots \\ \mathbf{W}_J \\ \mathbf{V}_J \end{pmatrix} = \begin{pmatrix} \mathcal{W}_1 \mathbf{X} \\ \mathcal{W}_2 \mathbf{X} \\ \mathcal{W}_3 \mathbf{X} \\ \vdots \\ \mathcal{W}_J \mathbf{X} \\ \mathcal{V}_J \mathbf{X} \end{pmatrix} \quad (19.10)$$

Each of the wavelet vectors \mathbf{W}_j ($j = 1, \dots, J$) has length $\frac{N}{2^j}$, has a time step of $2^j dt$, and corresponds to the filtering of the initial time series by a filter of nominal frequency band $[\frac{1}{dt2^{j+1}}; \frac{1}{dt2^j}]$. The scaling vector \mathbf{V}_J has length $\frac{N}{2^J}$, has a time step of $2^J dt$, and corresponds to the filtering of the initial time series by a filter of nominal frequency band $[0; \frac{1}{dt2^{J+1}}]$.

We can compute iteratively the wavelet vectors and the scaling vector using a pyramid algorithm and the wavelet filter h_l^o ($l = 0, \dots, N - 1$) and the scaling filter g_l^o ($l = 0, \dots, N - 1$):

$$W_{j,t} = \sum_{l=0}^{N-1} h_l^o V_{j-1,2t+1-l \mod N_{j-1}} \text{ and } V_{j,t} = \sum_{l=0}^{N-1} g_l^o V_{j-1,2t+1-l \mod N_{j-1}}, t = 0, \dots, N_j - 1 \quad (19.11)$$

where $N_j = \frac{N}{2^j}$ and $\mathbf{V}_0 = \mathbf{X}$.

We can then compute the j th level detail \mathbf{D}_j ($j = 1, \dots, J$), which is a vector of length N , defined by $\mathbf{D}_j = \mathcal{W}_j^T \mathbf{W}_j$ and the J th level smooth \mathbf{S}_J , which is a vector of length N , defined by $\mathbf{S}_J = \mathcal{V}_J^T \mathbf{V}_J$, and we get the multiresolution analysis (MRA) of \mathbf{X} :

$$\mathbf{X} = \sum_{j=1}^J \mathbf{D}_j + \mathbf{S}_J \quad (19.12)$$

One main advantage of the DWT is that it is an orthonormal transform, and thus we can write the analysis of variance (ANOVA):

$$\|\mathbf{X}\|^2 = \|\mathbf{W}\|^2 = \sum_{j=1}^J \|\mathbf{W}_j\|^2 + \|\mathbf{V}_J\|^2 = \sum_{j=1}^J \|\mathbf{D}_j\|^2 + \|\mathbf{S}_J\|^2 \quad (19.13)$$

Moreover, the DWT can be computed using $O(N)$ multiplications.

However, the DWT present several disadvantages:

- The length of the time series must be a multiple of 2^J where J is the level of the DWT decomposition.
- The time step of the wavelet vector \mathbf{W}_j is $2^j dt$, which may not correspond to the time when some interesting phenomenon is visible on the original time series.
- When we circularly shift the time series, the corresponding wavelet coefficients, details and smooths are not a circularly shifted version of the wavelet coefficients, details and smooths of the original time series. Thus, the values of the wavelet coefficients, details and smooths are strongly dependent on the time when we start experimentally gathering the data.
- When we filter the time series to obtain the details and smooths, we introduce a phase shift, which makes difficult to line up meaningfully the features of the MRA with the original time series.

To get rid of these problems, we introduce the Maximum Overlap Discrete Wavelet Transform (MODWT). The MODWT transforms the time series X_t ($t = 0, \dots, N - 1$) into J wavelet vectors $\tilde{\mathbf{W}}_j$ ($j = 1, \dots, J$) of length N and a scaling vector $\tilde{\mathbf{V}}_J$ of length N . Each wavelet vector $\tilde{\mathbf{W}}_j$ corresponds to the filtering of the original time series with a filter with nominal frequency band $[\frac{1}{dt2^{j+1}}; \frac{1}{dt2^j}]$. The scaling vector $\tilde{\mathbf{V}}_J$ corresponds to the filtering of the original time series with a filter with nominal frequency band $[0; \frac{1}{dt2^{j+1}}]$.

We can write the transformation as:

$$\tilde{\mathbf{W}}_j = \tilde{\mathcal{W}}_j \mathbf{X} \text{ and } \tilde{\mathbf{V}}_J = \tilde{\mathcal{V}}_J \mathbf{X} \quad (19.14)$$

$\tilde{\mathcal{W}}_j$ and $\tilde{\mathcal{V}}_J$ are related to \mathcal{W}_j and \mathcal{V}_J by:

$$\tilde{\mathcal{W}}_{j,tl} = \tilde{h}_{j,t-l \mod N}^o, \mathcal{W}_{j,tl} = h_{j,2^j(t+1)-1-l \mod N}^o \text{ and } \tilde{h}_{j,l}^o = \frac{h_{j,l}^o}{2^{j/2}} \quad (19.15)$$

As is the case for the DWT, we can compute iteratively the MODWT wavelet vectors and the scaling vector using a pyramid algorithm and the wavelet filter \tilde{h}_l^o ($l = 0, \dots, N - 1$) and the scaling filter \tilde{g}_l^o ($l = 0, \dots, N - 1$):

$$\tilde{\mathcal{W}}_{j,t} = \sum_{l=0}^{N-1} \tilde{h}_l^o V_{j-1,t-2^{j-1}l \mod N} \text{ and } \tilde{\mathcal{V}}_{j,t} = \sum_{l=0}^{N-1} \tilde{g}_l^o V_{j-1,t-2^{j-1}l \mod N}, t = 0, \dots, N - 1 \quad (19.16)$$

where $\tilde{h}_l^o = \frac{h_l^o}{\sqrt{2}}$ ($l = 0, \dots, N - 1$), $\tilde{g}_l^o = \frac{g_l^o}{\sqrt{2}}$ ($l = 0, \dots, N - 1$) and $\tilde{\mathbf{V}}_0 = \mathbf{X}$.

We can then compute the j th level detail $\tilde{\mathbf{D}}_j$ ($j = 1, \dots, J$), which is a vector of length N , defined by $\tilde{\mathbf{D}}_j = \tilde{\mathbf{W}}_j^T \tilde{\mathbf{W}}_j$ and the J th level smooth $\tilde{\mathbf{S}}_J$, which is a vector of length N , defined by $\tilde{\mathbf{S}}_J = \tilde{\mathcal{V}}_J^T \tilde{\mathbf{V}}_J$, and we get the multiresolution analysis (MRA) of \mathbf{X} :

$$\mathbf{X} = \sum_{j=1}^J \tilde{\mathbf{D}}_j + \tilde{\mathbf{S}}_J \quad (19.17)$$

and the ANOVA:

$$\|\mathbf{X}\|^2 = \sum_{j=1}^J \|\tilde{\mathbf{W}}_j\|^2 + \|\tilde{\mathbf{V}}_J\|^2 \quad (19.18)$$

Now, we have the following properties:

- The MODWT of a time series can be defined for any length N .
- The time step of the wavelet vectors $\tilde{\mathbf{W}}_j$ and the scaling vector $\tilde{\mathbf{V}}_J$ is equal to the time step of the original time series.
- When we circularly shift the time series, the corresponding wavelet vectors, scaling vector, details and smooths are shifted by the same amount.
- The details and smooths are associated with a zero phase filter, making it easy to line up meaningfully the features of the MRA with the original time series.

However, the MODWT has some disadvantages over the DWT:

- The MODWT can only be computed using $O(N \log_2 N)$ multiplications.

- We can no longer write the ANOVA for the details and smooths:

$$\|\mathbf{X}\|^2 \neq \sum_{j=1}^J \left\| \tilde{\mathbf{D}}_j \right\|^2 + \left\| \tilde{\mathbf{S}}_J \right\|^2 \text{ and } \left\| \tilde{\mathbf{W}}_j \right\|^2 \neq \left\| \tilde{\mathbf{D}}_j \right\|^2 \quad (19.19)$$

Chapter 20

Results

In the following, we show results of the DWT and MODWT analysis of one GPS time series.

Computing the DWT or the MODWT of a time series requires computing the convolution product of the time series with the wavelet or the scaling filter. To handle the boundary conditions, we assume that the time series is periodic, and extend accordingly the time series. However, we can only make this assumption when the discontinuity between the beginning and the end of the time series remains small. Therefore, we used the cleaned dataset in order to avoid discontinuities due to the linear trend, and earthquakes or hardware upgrades. In order to analyze the temporal correlation of the slow slip with the tectonic tremor, we also used the tremor catalog of the Pacific Northwest Seismic Network (PNSN, Wech, 2010 [49]) to get the cumulative number of tremor recorded around the GPS station. The displacement is recorded once a day at every GPS station. However, there are many missing data points. We chose the GPS station PGC5, located in southern Vancouver Island, near Victoria. The slow slip events are clearly visible in the longitudinal component of the displacement (see bottom panel of Figure 20.1). Moreover, there are very few missing data for this station. In the following, we have analyzed eight years of GPS data from 2006 to 2014. There are only five days for which the displacement is missing. We replaced the missing data by the average of the displacement on the day before and the displacement on the day after.

We first carried out a partial DWT of the time series. To choose the appropriate wavelet filter, we computed the Normalized Partial Energy Sequence (NPES) of the wavelet coefficients and of the time series for different wavelet filters. It did not seem that there was much difference between the different wavelet filters. In the following, we will compare the wavelet coefficients to the cumulative number of tremor recorded around the GPS station. Therefore, we would like to know with good precision the time shift that should be applied to the wavelet coefficients. Moreover, we would like the length of the wavelet filter to remain small, in order to reduce the number of coefficients that are affected by the interpolation we had to do to replace the missing data. This is why we chose the Daubechies least asymmetric (LA8) wavelet filter in the following analysis.

The total duration of a slow slip event is about six weeks. Therefore, we only carried out a partial DWT up to the level 6 (corresponding to a scale of 64 days), because we do not expect to see features at a longer scale in the time series.

The wavelet coefficients for level 1 to 6 are shown in Figure 20.1. The red bars correspond to the days where data were missing. The grey bars correspond to the timing of ETS events. The blue bars correspond to the left and right boundaries outside of which the wavelet coefficients are affected by the boundary conditions. We can clearly see big wavelet coefficients corresponding to the January 2007 ETS event at the levels 5 and 6, to the May 2009 ETS event at the level 5, to the August 2010 ETS event at the level 6, to the September 2012 ETS event at the levels 5 and 6, and to the September 2013 ETS event at the levels 5 and 6. The May 2008 and August 2011 ETS events are not clearly seen in the wavelet coefficients.

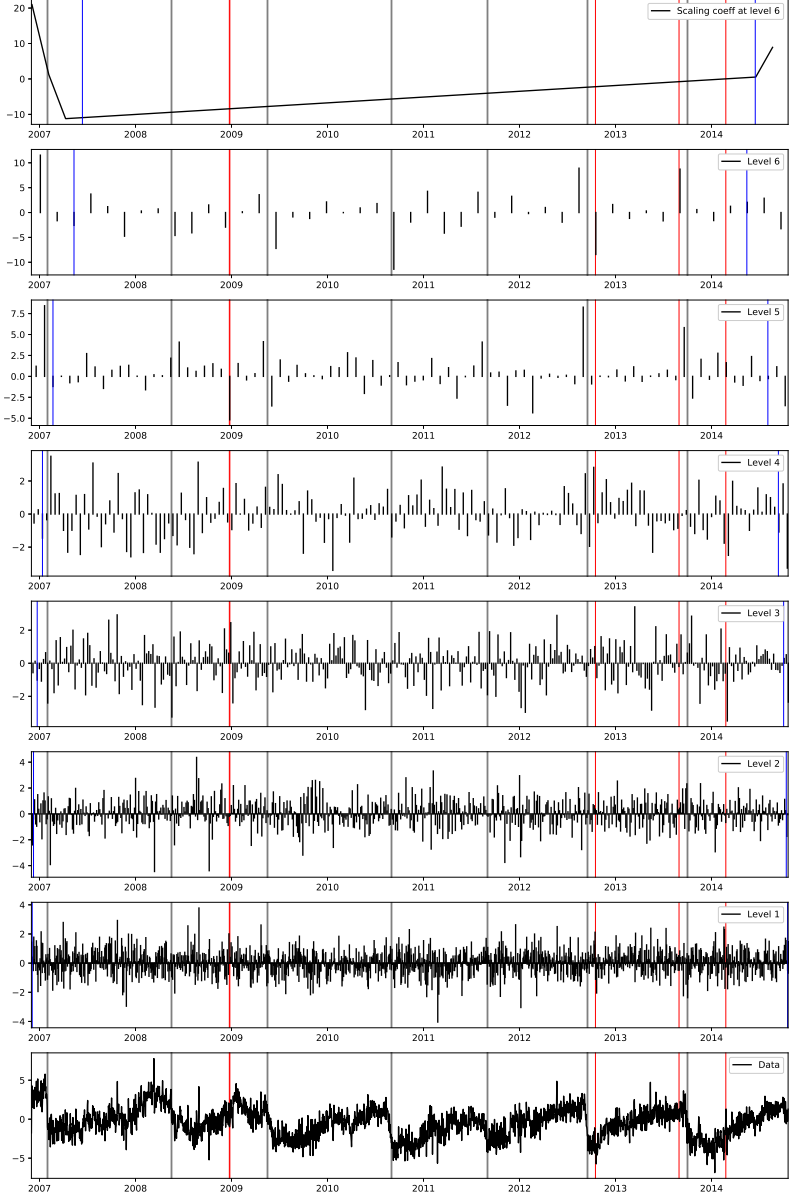


Figure 20.1: Partial DWT wavelet coefficients up to level 6 of the longitudinal component of station PGC5. The red bars correspond to the days where data were missing. The grey bars correspond to the timing of ETS events. The blue bars correspond to the left and right boundaries outside of which the wavelet coefficients are affected by the boundary conditions.

The 5th and 6th level details of the MRA are plotted with the cumulative number of tremor in Figure 20.2. Unfortunately, the tremor catalog from the PNSN website only starts in August 2009. We plotted successively the cumulative number of tremor which source was located less than 20, 40, 60, 80, or 100 kilometres from the GPS station. We can clearly see the August 2010, September 2012 and September 2013 ETS events in the 6th level detail. The August 2011 ETS event is less obvious, but can be seen in the 5th level detail. There is a small increase in the number of tremor in March 2010, but it is not really clear that there is a corresponding peak in the 5th level detail.

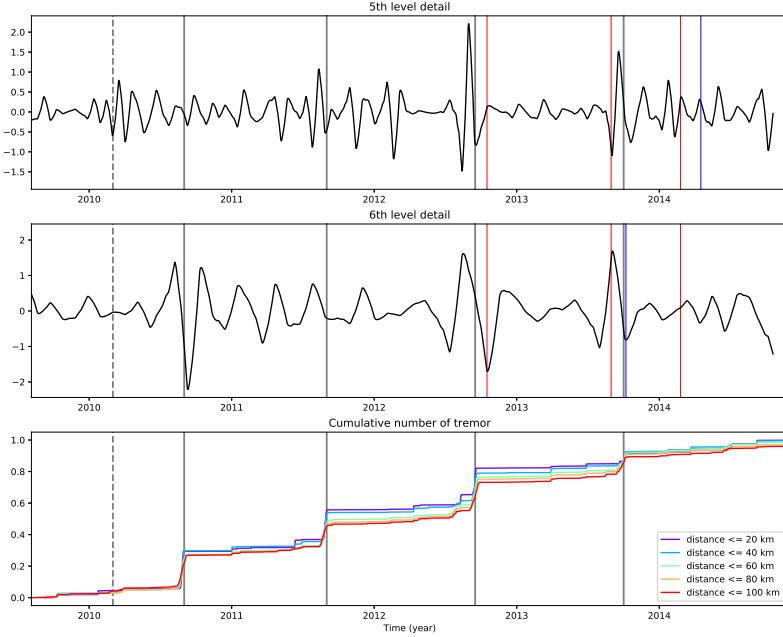


Figure 20.2: 5th and 6th level details of the partial DWT analysis of the longitudinal component of station PGC5 (top and middle panel), and cumulative number of tremor recorded around the GPS station (bottom panel). The red bars correspond to the days where data were missing. The grey bars correspond to the timing of ETS events. The blue bar corresponds to the right boundary outside of which the wavelet coefficients are affected by the boundary conditions.

The details of the MRA with the partial DWT have a somewhat 'shark fin' look, which is not entirely pleasing. Moreover, the number of days between two ETS events may not correspond to a multiple of a power of 2. Therefore, it would be easier to interpret the wavelet coefficients at each level if their dimensions was the same as the dimension of the original time series. Finally, it would be easier to associate the details and smooths of the MRA with the cumulative number of tremor recorded if they were associated with zero phase filters. Therefore, in the following, we carried out a MODWT analysis on the same time series.

The wavelet coefficients for level 1 to 6 are shown in Figure 20.3. We can clearly see peaks corresponding to the January 2007, May 2009, August 2010, September 2012, and September 2013 ETS events in both the level 5 and level 6 coefficients. A peak corresponding to the May 2008 ETS event can be seen in the level 5 coefficients. However, it is still difficult to observe the August 2011 ETS event in the wavelet coefficients.

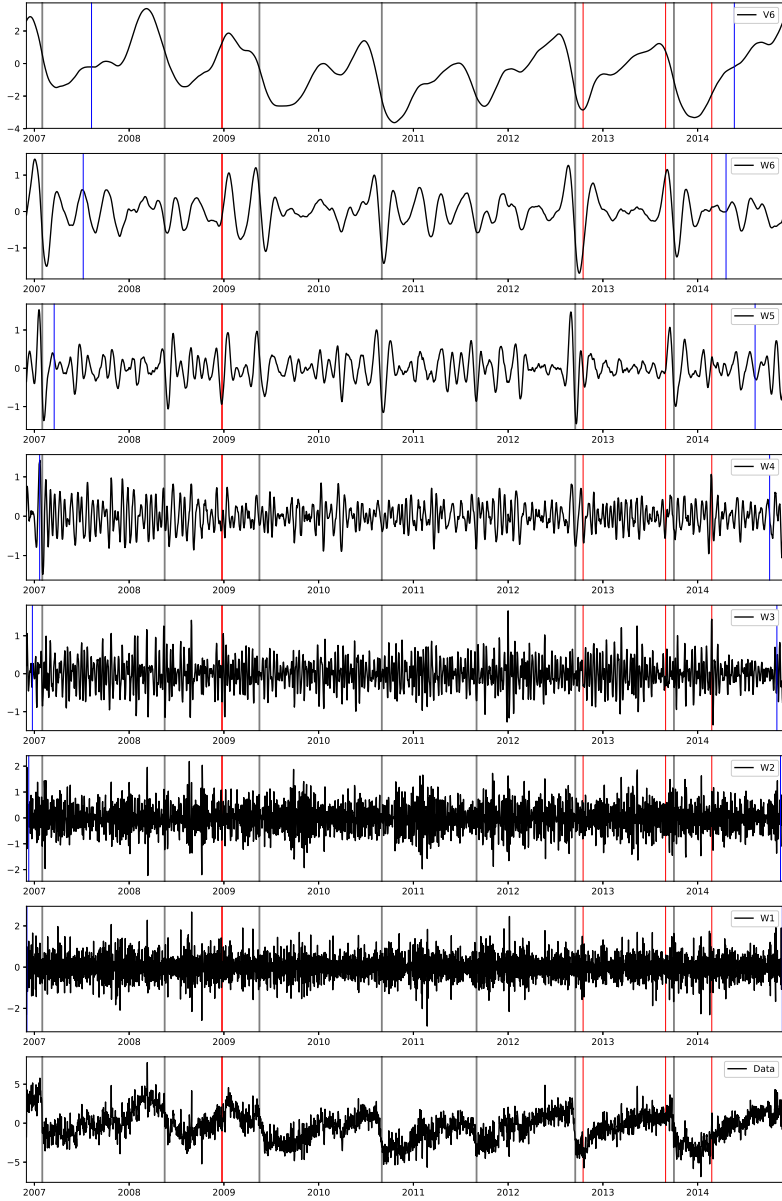


Figure 20.3: Partial MODWT wavelet coefficients up to level 6 of the longitudinal component of station PGC5. The red bars correspond to the days where data were missing. The grey bars correspond to the timing of ETS events. The blue bars correspond to the left and right boundaries outside of which the wavelet coefficients are affected by the boundary conditions.

Finally, the 5th and 6th level details of the MRA are plotted with the cumulative number of tremor in Figure 20.4. Peaks corresponding to the August 2010, September 2012 and September 2013 ETS events can clearly be seen in both the 5th and the 6th level details. Peaks that could correspond to the August 2011 ETS event, and a small inter-ETS event in March 2010, can also be seen in the 5th level detail, but this is less obvious than for the other ETS events.

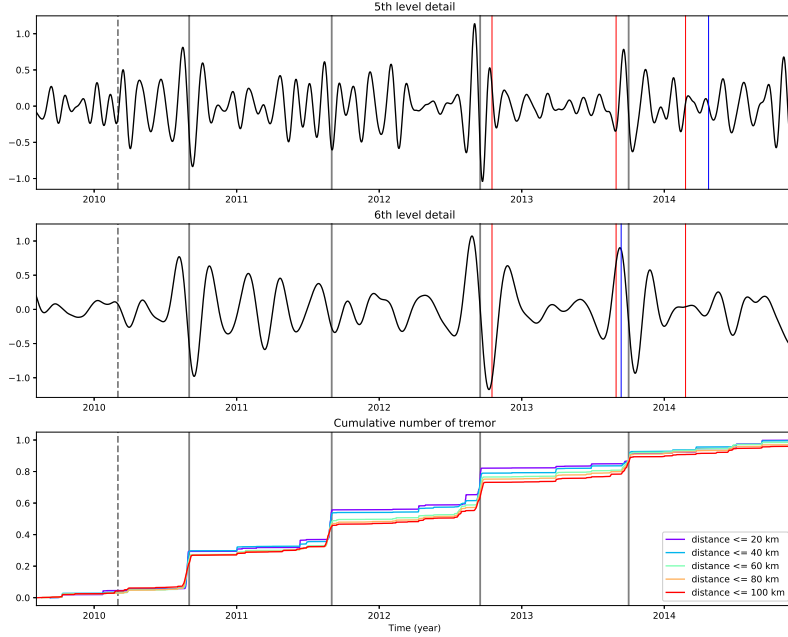


Figure 20.4: 5th and 6th level details of the partial MODWT analysis of the longitudinal component of station PGC5 (top and middle panel), and cumulative number of tremor recorded around the GPS station (bottom panel). The red bars correspond to the days where data were missing. The grey bars correspond to the timing of ETS events. The blue bar corresponds to the right boundary outside of which the wavelet coefficients are affected by the boundary conditions.

We did a similar analysis with the longitudinal component of the displacement at GPS stations CLRS, CUSH, FRID, PNCL, PTAA, and SQIM, all located in the Olympic Peninsula, or on Vancouver Island, and we found similar results. The 5th and 6th level details of the MRA for each of these stations is plotted as function of the latitude of the stations in Figures 20.5 and 20.6. For the 5th level detail, we can see a peak corresponding to the August 2010 ETS event for stations FRID, PNCL, SQIM, and CUSH. The September 2012 ETS event can be seen for stations CLRS, PGC5, PTAA, and CUSH. The September 2013 ETS event can be seen for stations CLRS, PGC5, and PTAA. The January 2016 ETS event can be seen for stations CLRS, PGC5, FRID, PTAA, and CUSH. Finally, the March 2017 ETS event can be seen for stations CLRS, PGC5, and PTAA.

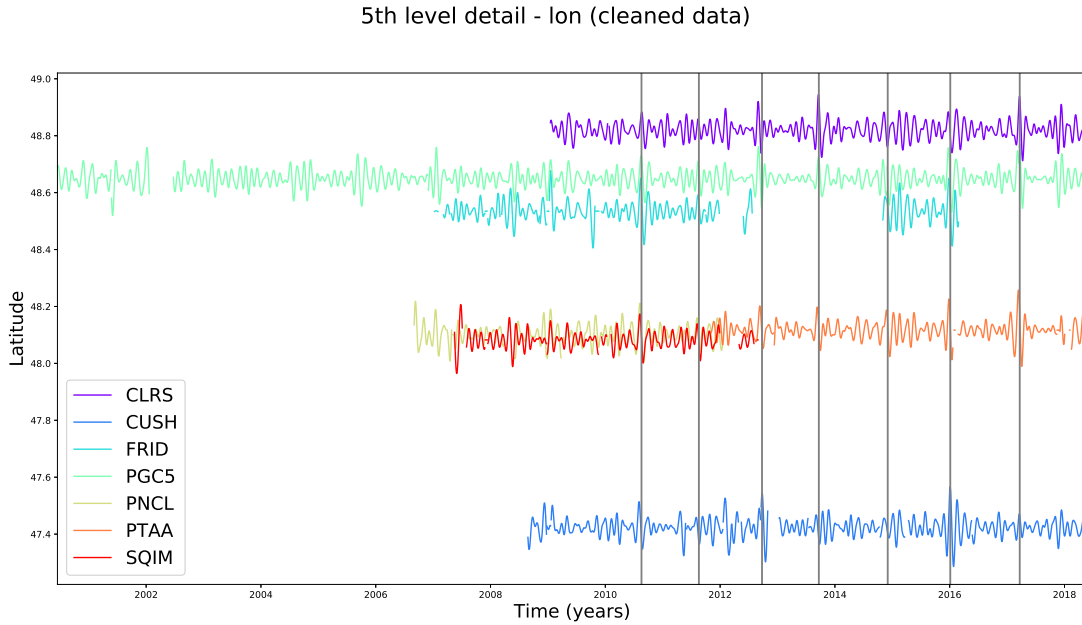


Figure 20.5: 5th level detail of the partial MODWT analysis for GPS stations CLRS, CUSH, FRID, PGC5, PNCL, PTAA, and SQIM, as function of the latitude of the stations. The grey bars correspond to the timing of ETS events.

For the 6th level detail, we can see a peak corresponding to the August 2010 ETS event for stations PGC5, FRID, PNCL, and SQIM. The September 2012 ETS event can be seen for stations CLRS, PGC5, and PTAA. The September 2013 ETS

event can be seen for stations CUSH, PGC5, and PTAA. The December 2014 ETS event can be seen for stations FRID, and PTAA. Finally, the January 2016 ETS event can be seen for stations PGC5, and FRID.

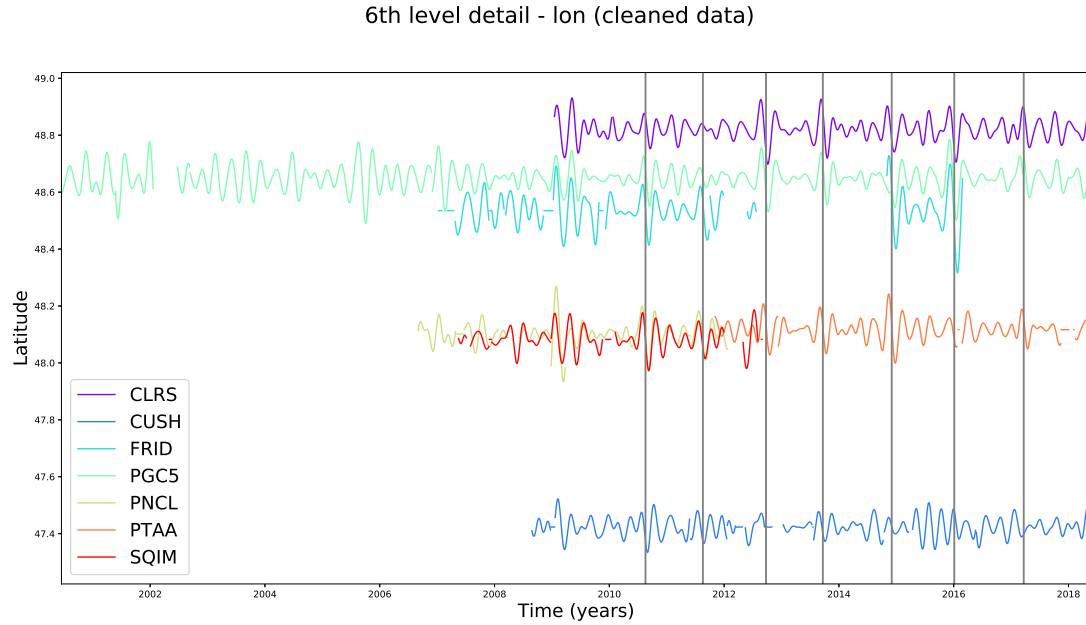


Figure 20.6: 6th level detail of the partial MODWT analysis for GPS stations CLRS, CUSH, FRID, PGC5, PNCL, PTAA, and SQIM, as function of the latitude of the station. The grey bars correspond to the timing of ETS events.

Chapter 21

Discussion and things to do

Things to do:

- Change point detection: Can we detect a big ETS event starting, and when can we detect it? Before it becomes obvious due to the tremor recordings? We could test other wavelets (Daubechies with extremal phase may be a good idea), or look at the wavelet variance (see paper by Eric Moulines - Kouamo et al., 2011, with correction of the mistake in Percival's paper).
- Plot of the cumulative number of tremor: How to get the exact timing of the inflection point / change point for putting it on the wavelet plot?
- Implementation of matching pursuit: I hope to see among the first basis vectors the ones at level 5 and 6 that could correspond to the big ETS events, and maybe some others at level 4 that could correspond to smaller and shorter inter-ETS events.
- Looking at what could do for the missing data points:
 - Linear or more complex interpolation
 - Simply replace them with Gaussian noise
 - Look at what we can do with kriging
- Doing a test with a synthetics time series, and look at what we can see (level where we see the slow slip compared with duration, influence of an outlier, missing data, noise, influence of different types of wavelets)
- Test other wavelets with MODWT details
- Regions to look at: New Zealand (slow slip but no tremor), Alaska (5 years long slow slip events)
- For NASA fellowship, see Scott Henderson and glaciology students + speak about three points:
 - The science
 - The societal aspect (natural hazards)
 - The technique: the idea is to develop a method, exploit GPS data, pull out signals, make it more useful, maybe it could be applied to other types of phenomena

21.1 Broader impacts

Broader impacts = Answer to the following questions:

- Societal benefit, improve life on our planet, assess and respond to natural hazards and extreme events, inform decisions and provide benefits to society
- Develop a method, exploit GPS data, pull out signals, make it more useful
- Emphasis on the utilization of NASA's unique capabilities (fleet of Earth observing satellite)
- Science + societal + techniques
- Other types of phenomena that could be analyzed with the same methods

21.1.1 Better understanding of the seismic hazard

The largest earthquakes on Earth occur in subduction zones, where large segments of the plate boundary can store energy for centuries and then release it in minutes. A better understanding of subduction zone processes is thus necessary to study the associated seismic hazard. Moreover, slow slip and tremor events have a relatively short recurrence time, compared to the earthquake cycle that can last for hundreds of years, allowing scientists to observe and study complete event cycles, which are typically not possible to explore with traditional earthquake catalogs. Finally, slow slip occurs in a section of the plate boundary adjacent to the locked section of the subduction zone. This transient motion thus complicates our understanding of the earthquake cycle, as interactions between the slow slip zone and the seismogenic zone could potentially trigger large earthquakes, and should be taken into account when studying the seismic hazard.

Specifically, a better measurement of the vertical displacement at the Earth's surface during slow slip events is necessary to better constrain the depth extent of the slip area at the plate boundary. The up-dip limit of the slow slip area is assumed to constrain the down-dip limit of the megathrust earthquake rupture, a variable that is useful for seismic hazard studies, and the design of building codes. Constraining the down-dip limit of slow slip is also useful to estimate the area that slips during a slow-motion earthquake, and thus the percentage of the plate convergence that is released by large slow slip episodes. Additionally, the up-dip and down-dip limits of slow slip can be correlated with other geophysical data, such as porosity, temperature, and structure, in an effort to better understand the underlying processes that facilitate aseismic slip.

Moreover, being able to detect smaller, currently undetected slow slip events would help us to verify whether the fault weakens with depth. Indeed, it has been observed that, with increasing depth, there is a gradation from frequent tremor episodes with small spatial and temporal extent, to infrequent tremor episodes with large spatial and temporal extent. The same behavior was observed for low-frequency earthquakes (LFEs) with downdip LFE swarms happening nearly weekly and up-dip families only occurring during the yearly Episodic Tremor and Slip (ETS) events. As there is a temporal and spatial correlation between slow slip, tremor and LFEs, the same spatial pattern is also expected for the slow slip. However, the limited resolution of geodetic instruments only allows us to observe the largest slow slip events, and many smaller slow slip events may be undetected. It has been hypothesized that stable sliding at depth transfers stress to the base of the ETS zone, initiating frequent tremor and small slow slip. In a self-similar process, stress is then transferred up-dip of the fault, triggering less frequent tremor and larger slow slip, up toward the locked zone. This unobserved up-dip slip could help mediate plate convergence and either lower the slip deficit available for co-seismic slip or shift the downward extent of the megathrust rupture away from urban centers.

21.1.2 Extension of the method to the study of other phenomena

One of the main objectives of this research project is to develop a wavelet method to carry out analyses of GPS time series, and make GPS datasets more helpful for the study of physical phenomena.

Indeed, wavelet methods combined with GPS measurements have already been used for instance for monitoring bridge deformation. Kaloop and Li (2015 [24]) used the Discrete Wavelet Transform to detect abrupt changes in the GPS response by decomposing the signal into approximation and detail levels. Wavelet methods are also used for noise reduction of GPS observations, and improvement of the accuracy of the GPS time series (Kaloop and Kim, 2016 [23]).

It is important to monitor the displacement time series and to explore the failure mechanism of reservoir landslide for early warning. Traditionally, it is a challenge to monitor the landslide displacements real-timely and automatically. Globe Position System (GPS) is considered as the best real-time monitoring technology, however, the accuracies of the landslide displacements monitored by GPS are not assessed effectively. A web-based GPS system is developed to monitor the landslide displacements real-timely and automatically in this study. And the discrete wavelet transform (DWT) is proposed to assess the accuracy of the GPS monitoring displacements. In this study, the wavelet analysis (WA) is proposed to assess the accuracy of the GPS monitoring landslide displacements. A web-based GPS system for displacement monitoring and failure mechanism analysis of reservoir landslide Li, Yuanyao ; Huang, Jinsong ; Jiang, Shui-Hua ; Huang, Faming ; Chang, Zhiyu Sci Rep, 2017, Vol.7(1), pp.17171-17171

develop a robust GPS signal acquisition system that improves the performance of the system over noisy transmission channel and in the presence of other sources of noise. An acquisition algorithm based on DWT is proposed for a robust GPS signal acquisition system and to facilitate its implementation. Acquisition is the first signal processing operation performed on the IF GPS signal. Acquisition identifies the satellites visible to the receiver and provides the estimation of the Doppler shift in carrier frequency and delay in C/A code of the satellite signals. These parameters are given as input to the tracking, is used to find the phase transition of the navigation data. After identifying the available satellites and acquiring their signal parameters, tracking is done through parallel channels. In tracking, C/A code and carrier are removed by measurement of the code phase and Doppler frequency precisely. So performance of acquisition processes directly influence the performance

of tracking operation. The most affecting source of acquisition error is due to the noise on the transmission channel. The presence of the noise affects seriously the precision in the measurements of acquisition process. A Robust GPS Signal Acquisition Technique Using Discrete Wavelet Transform Ahamed, Shaik Fayaz ; Rao, G. Sasibhushana ; Ganesh, L. Procedia Computer Science, 2016, Vol.85, pp.683-690

Repeatable satellite orbits can be used for multipath mitigation in GPS-based deformation monitoring and other high-precision GPS applications that involve continuous observation with static antennas. Multipath signals at a static station repeat when the GPS constellation repeats given the same site environment. Repeat-time multipath filtering techniques need noise reduction methods to remove the white noise in carrier phase measurement residuals in order to retrieve the carrier phase multipath corrections for the next day. We propose a generic and robust three-level wavelet packets based denoising method for repeat-time-based carrier phase multipath filtering in relative positioning; the method does not need tuning to work with different data sets.

Wavelet packets based denoising method for measurement domain repeat-time multipath filtering in GPS static high-precision positioning Lau, Lawrence GPS Solutions, 2017, Vol.21(2), pp.461-474

Multipath remains one of the major challenges in Global Navigation Satellite System (GNSS) positioning because it is considered the dominant source of ranging errors. Urban situations in particular are affected by this phenomenon, yielding several blunders in the measurements and unacceptable errors in the navigation solution. Multipath is caused by multiple signal reflections from various objects in the environment; multipath signals are always delayed compared to line-of-sight signals. Multipath remains one of the major challenges in Global Navigation Satellite System (GNSS) positioning because it is considered the dominant source of ranging errors, which can be classified into specular and diffuse types. We present a new method using wavelets to extract the pseudorange multipath in the time domain and breaking it down into the two components. The main idea is an analysis-reconstruction approach based on application of both continuous wavelet transform (CWT) and discrete wavelet transform (DWT). A new method for specular and diffuse pseudorange multipath error extraction using wavelet analysis Pugliano, Giovanni ; Robustelli, Umberto ; Rossi, Fabio ; Santamaria, Raffaele GPS Solutions, 2016, Vol.20(3), pp.499-508

GPS uses a direct sequence spread-spectrum (DSSS) signal that is highly susceptible to interference, which may be both intentional and nonintentional. The primary area of concern in both commercial and military applications is the protection from intentional interferers. Development of techniques for the protection of GPS from interference and jamming is an area of active research. Hence, a discrete wavelet transform (DWT) filter using a biorthogonal wavelet is suggested and its performance analyzed here for single and multiple FM (frequency modulation) interference suppression. New approach for suppression of FM jamming in GPS receivers Deergha Rao, K. ; Swamy, M.N.S. IEEE Transactions on Aerospace and Electronic Systems, October 2006, Vol.42(4)

21.1.3 Data management

All scripts used to carry out the wavelet analysis and generate the figures are written with Python, and are available on the student's GitHub repository. Jupyter notebooks explaining in a more detailed manner the wavelet analysis are also available on GitHub. All future scripts developed during this research project will be made available to the public in a similar way.

Part VII

Long-range dependence

Chapter 22

Data

22.1 LFE catalogs

The Chestler catalog

The Plourde catalog The catalog of Plourde *et al.* (2015 [36]) contains event times for 66 templates corresponding to 34 families located in Southern Cascadia. They were established using the seismic stations from the EarthScope Flexible Array Mendocino Experiment (FAME) array, and seven permanent stations from the Northern California Seismic Network. The period covered starts on March 21st 2008, and ends on April 30th 2008, which corresponds to the main 2008 ETS event in southern Cascadia. Unfortunately, we do not have (yet) the event times for the three LFE families located on the Maacama and Bucknell Creek faults, which are part of the San Andreas fault zone.

The Shelly catalog

The Sweet catalog

Chapter 23

Method

Chapter 24

Results

Chapter 25

Discussion and things to do

In David Shelly's LFE catalog, do we have a lower rate of LFEs when the number of stations decreases (at the end of the dataset)?

Can we find a daily periodicity in the LFE catalog because of cultural noise?

The aggregation of short-range dependence time series can lead to a long-range dependence time series (see Jan Beran's book page 14, and a paper by Granger). Could an ETAS model with correlation between asperities lead to a model with long-range dependence?

Bibliography

- [1] K. Aki and P.G. Richards. *Quantitative Seismology*. University Science Books, 2nd edition edition, 2002.
- [2] Sequoia Alba. ETS in tidal records. Master's thesis, University of Oregon, December 2011.
- [3] J.G. Armbruster, W.Y. Kim, and A.M. Rubin. Accurate tremor locations from coherent S and P waves. *Journal of Geophysical Research: Solid Earth*, 119:5000–5013, 2014. doi:10.1002/2014jb011133.
- [4] P. Audet, M.G. Bostock, N.I. Christensen, and S.M. Peacock. Seismic evidence for overpressure subducted oceanic crust and mega thrust fault sealing. *Nature*, 457:76–78, January 2009. doi:10.1038/nature07650.
- [5] G. Blewitt and D. Lavallée. Effects of annual signals on geodetic velocity. *Journal of Geophysical Research*, 107:B72145, 2002. doi:10.1029/2001jb000570.
- [6] M.G. Bostock. The Moho in subduction zones. *Tectonophysics*, 609:547–557, 2013. doi:10.1016/j.tecto.2012.07.007.
- [7] M.G. Bostock, A.A. Royer, E.H. Hearn, and S.M. Peacock. Low frequency earthquakes below southern Vancouver Island. *Geochemistry Geophysics Geosystems*, 13(11):Q11007, November 2012. doi:10.1029/2012gc004391.
- [8] M.G. Bostock, A.M. Thomas, G. Savard, L. Chuang, and A.M. Rubin. Magnitudes and moment-duration scaling of low frequency earthquakes beneath southern Vancouver Island. *Journal of Geophysical Research: Solid Earth*, 120:6329–6350, 2015. doi:10.1002/2015jb012195.
- [9] S.R. Chestler and K.C. Creager. Evidence for a scale-limited low-frequency earthquake source process. *Journal of Geophysical Research: Solid Earth*, 122:3099–3114, 2017. doi:10.1002/2016jb013717.
- [10] S.R. Chestler and K.C. Creager. A model for low-frequency earthquake slip. *Geochemistry, Geophysics, Geosystems*, 18:4690–4708, 2017. doi:10.1002/2017gc007253.
- [11] H. Dragert, K. Wang, and T.S. James. A silent slip event on the deeper Cascadia subduction interface. *Science*, 292:1525–1528, May 2001. doi:10.1126/science.1060152.
- [12] H. Dragert, K. Wang, and G. Rogers. Geodetic and seismic signatures of episodic tremor and slip in the northern Cascadia subduction zone. *Earth Planets Space*, 56:L23602, 2004.
- [13] W.B. Frank, N.M. Shapiro, A.L. Husker, V. Kostoglodov, A.A. Gusev, and M. Campillo. The evolving interaction of low-frequency earthquakes during transient slip. *Science Advances*, 2(4):e1501616, April 2016. doi:10.1126/sciadv.1501616.
- [14] H. Gao, D.A. Schmidt, and R.J. Weldon. Scaling relationships of source parameters for slow slip events. *Bulletin of the Seismological Society of America*, 102(1):352–360, February 2012. doi:10.1785/0120110096.
- [15] A. Ghosh, J.E. Vidale, and K.C. Creager. Tremor asperities in the transition zone control evolution of slow earthquakes. *Journal of Geophysical Research*, 117:B10301, 2012. doi:10.1029/2012jb009249.
- [16] A. Ghosh, J.E. Vidale, J.R. Sweet, K.C. Creager, A.G. Wech, and H. Houston. Rapid, continuous streaking of tremor in Cascadia. *Geochemistry, Geophysics, Geosystems*, 11(12):Q12010, December 2010. doi:10.1029/2010gc003305.
- [17] J. Gomberg, A. Wech, K. Creager, K. Obara, and D. Agnew. Reconsidering earthquake scaling. *Geophysical Research Letters*, 43:6243–6251, 2016. doi:10.1002/2016gl069967.
- [18] H. Houston. Low friction and fault weakening revealed by rising sensitivity of tremor to tidal stress. *Nature Geoscience*, 8(5):409–415, May 2015. doi:10.1038/ngeo2419.
- [19] R.D. Hyndman, P.A. McCrory, A. Wech, H. Kao, and J. Ague. Cascadia subducting plate fluids channelled to fore-arc mantle corner: ETS and silica deposition. *Journal of Geophysical Research: Solid Earth*, 120:4344–4358, 2015. doi:10.1002/2015jb011920.

- [20] S. Ide, G.C. Beroza, D.R. Shelly, and T. Uchide. A scaling law for slow earthquakes. *Nature*, 447:76–79, May 2007. doi:10.1038/nature05780.
- [21] S. Ide, D.R. Shelly, and G.C. Beroza. Mechanism of deep low frequency earthquakes: Further evidence that deep non-volcanic tremor is generated by shear slip on the plate interface. *Geophysical Research Letters*, 34:L03308, 2007. doi:10.1029/2006gl028890.
- [22] K. Idehara, S. Yabe, and S. Ide. Regional and global variations in the temporal clustering of tectonic tremor activity. *Earth, Planets and Space*, 66(1):1–10, 2014. doi:10.1186/1880-5981-66-66.
- [23] M.R. Kaloop and D. Kim. De-noising of GPS structural monitoring observation error using wavelet analysis. *Geomatics, Natural Hazards and Risk*, 7(2):804–825, 2016. doi:10.1080/19475705.2014.983186.
- [24] M.R. Kaloop and H. Li. Sensitivity and analysis GPS signals based bridge damage using GPS observations and wavelet transform. *Measurement*, 44(5):927–937, 2011. doi:10.1016/j.measurement.2011.02.008.
- [25] M. La Rocca, K.C. Creager, D. Galluzzo, S. Malone, J.E. Vidale, J.R. Sweet, and A.G. Wech. Cascadia tremor located near plate interface constrained by S minus P wave times. *Science*, 323:620–623, January 2009. doi:10.1126/science.1167112.
- [26] P.A. McCrory, J.L. Blair, D.H. Oppenheimer, and S.R. Walter. Depth to the Juan de Fuca slab beneath the Cascadia subduction margin - a 3-D model sorting earthquakes. Technical Report Series 91, U.S. Geological Survey, 2006. ISBN: 0-607-97922-4.
- [27] T.I. Melbourne, W.M. Szeliga, M.M. Miller, and V.M. Santillan. Extent and duration of the 2003 Cascadia slow earthquake. *Geophysical Research Letters*, 32:L04301, 2005. doi:10.1029/2004gl021790.
- [28] M.M. Miller, T. Melbourne, D.J. Johnson, and W.Q. Sumner. Periodic slow earthquakes from the Cascadia subduction zone. *Science*, 295(5564):2423, March 2002.
- [29] Rosanne Nikolaids. *Observation of geodetic and seismic deformation with the Global Positioning System*. PhD thesis, University of California, San Diego, 2002.
- [30] A. Nikulin, V. Levin, and J. Park. Receiver function study of the Cascadia megathrust: Evidence for localized serpen-tinization. *Geochemistry, Geophysics, Geosystems*, 10:Q07004, 2009. doi:10.1029/2009GC002376.
- [31] R.L. Nowack and M.G. Bostock. Scattered waves from low-frequency earthquakes and plate boundary structure in northern Cascadia. *Geophysical Research Letters*, 40:4238–4243, 2013. doi:10.1002/grl.50826.
- [32] K. Obara. Nonvolcanic deep tremor associated with subduction in southwest Japan. *Science*, 296(5573):1679–1681, May 2002.
- [33] K. Obara, H. Hires, F. Yamamizu, and K. Kasahara. Episodic slow slip events accompanied by non-volcanic tremors in southwest Japan subduction zone. *Geophysical Research Letters*, 31:1143–1150, 2004. doi:10.1029/2004gl020848.
- [34] R. Ohtani, J.J. McGuire, and P. Segall. Network strain filter: A new tool for monitoring and detecting transient deformation signals in GPS arrays. *Journal of Geophysical Research*, 115:B12418, 2010.
- [35] D.B. Percival and A.T. Walden. *Wavelet Methods for Time Series Analysis*. Cambridge Series in Statistical and Probabilistic Mathematics. Cambridge University Press, New York, NY, USA, 2000.
- [36] A.P. Plourde, M.G. Bostock, P. Audet, and A.M. Thomas. Low-frequency earthquakes at the southern Cascadia margin. *Geophysical Research Letters*, 42:4849–4855, 2015. doi:10.1002/2015gl064363.
- [37] L.A. Preston, K.C. Creager, R.S. Crosson, T.M. Brocher, and A.M. Trehu. Intralab earthquakes: Dehydration of the Cascadia slab. *Science*, 302(5648):1197–1200, November 2003.
- [38] G. Rogers and H. Dragert. Tremor and slip on the Cascadia subduction zone: The chatter of silent slip. *Science*, 300(5627):1942–1943, June 2003.
- [39] A.A. Royer and M.G. Bostock. A comparative study of low frequency earthquake templates in northern Cascadia. *Earth and Planetary Science Letters*, 402:247–256, 2014. doi:10.1016/j.epsl.2013.08.040.
- [40] F.J. Sánchez-Sesma and M. Campillo. Retrieval of the Green's function from cross correlation: The canonical elastic problem. *Bulletin of the Seismological Society of America*, 96(3):1182–1191, June 2006. doi:10.1785/0120050181.
- [41] D.A. Schmidt and H. Gao. Source parameters and time-dependent slip distributions of slow slip events on the Cascadia subduction zone from 1998 to 2008. *Journal of Geophysical Research*, 115:B00A18, 2010. doi:10.1029/2008jb006045.

- [42] D.R. Shelly. A 15 year catalog of more than 1 million low-frequency earthquakes: Tracking tremor and slip along the deep San Andreas fault. *Journal of Geophysical Research. Solid Earth*, 122:3739–3753, 2017. doi:10.1002/2017jb014047.
- [43] D.R. Shelly, G.C. Beroza, and S. Ide. Non-volcanic tremor and low-frequency earthquake swarms. *Nature*, 446:305–307, March 2007. doi:10.1038/nature05666.
- [44] D.R. Shelly, G.C. Beroza, S. Ide, and S. Nakamura. Low-frequency earthquakes in Shikoku, Japan, and their relationship to episodic tremor and slip. *Nature*, 442:188–191, July 2006. doi:10.1038/nature04931.
- [45] D.R. Shelly and J.L. Hardebeck. Precise tremor source locations and amplitude variations along the lower-crustal central San Andreas Fault. *Geophysical Research Letters*, 37:L14301, 2010. doi:10.1029/2010gl043672.
- [46] W. Szeliga, T. Melbourne, M. Santillan, and M. Miller. Gps constraints on 34 slow slip events within the Cascadia subduction zone, 1997-2005. *Journal of Geophysical Research*, 113:B04404, 2008. doi:10.1029/2007jb004948.
- [47] W. Szeliga, T.I. Melbourne, M.M. Miller, and V.M. Santillan. Southern Cascadia episodic slow earthquakes. *Geophysical Research Letters*, 31:L16602, 2004. doi:10.1029/2004GL020824.
- [48] C.H. Thurber, X. Zeng, A.M. Thomas, and P. Audet. Phase-weighted stacking applied to low-frequency earthquakes. *Bulletin of the Seismological Society of America*, 104(5):2567–2572, October 2014. doi:10.785/0120140077.
- [49] A.G. Wech. Interactive tremor monitoring. *Seismological Research Letters*, 81(4):664–669, July-August 2010. doi:10.1785/gssrl.81.4.664.
- [50] A.G. Wech and K.C. Creager. Automated detection and location of Cascadia tremor. *Geophysical Research Letters*, 35:L20302, 2008. doi:10.1029/2008gl035458.
- [51] A.G. Wech and K.C. Creager. A continuum of stress, strength and slip in the Cascadia subduction zone. *Nature Geoscience*, 4(9):624–628, August 2011. doi:10.1038/ngeo1215.
- [52] M. Wei, J.J. McGuire, and E. Richardson. A slow slip event in the south central Alaska Subduction Zone. *Geophysical Research Letters*, 39:L15309, 2012. doi:10.1029/2012gl052351.